

CAPTURE AND EVOLUTION OF PLANETESIMALS IN CIRCUMJOVIAN DISKS

GENNARO D'ANGELO^{1,2} AND MORRIS PODOLAK³

The Astrophysical Journal, in press

ABSTRACT

We study the evolution of planetesimals in evolved gaseous disks, which orbit a solar-mass star and harbor a Jupiter-mass planet at $a_p \approx 5$ AU. The gas dynamics is modeled with a three-dimensional hydrodynamics code that employs nested-grids and achieves a resolution of one Jupiter's radius in the circumplanetary disk. The code models solids as individual particles. Planetesimals are subjected to gravitational forces by the star and the planet, drag force by the gas, disruption via ram pressure, and mass loss through ablation. The mass evolution of solids is calculated self-consistently with their temperature, velocity, and position. We consider icy and icy/rocky bodies of radius 0.1–100 km, initially deployed on orbits around the star within a few Hill radii (R_H) of the planet's orbit. Planetesimals are scattered inward, outward, and toward disk regions of radius $r \gg a_p$. Scattering can relocate significant amounts of solids, provided that regions $|r - a_p| \sim 3 R_H$ are replenished with planetesimals. Scattered bodies can be temporarily captured on planetocentric orbits. Ablation consumes nearly all solids at gas temperatures $\gtrsim 220$ K. Super-keplerian rotation around and beyond the outer edge of the gas gap can segregate $\lesssim 0.1$ km bodies, producing solid gap edges at size-dependent radial locations. Capture, break-up, and ablation of solids result in a dust-laden circumplanetary disk with low surface densities of km-size planetesimals, implying relatively long timescales for satellite formation. After a giant planet acquires most of its mass, accretion of solids is unlikely to alter significantly its heavy-element content. The luminosity generated by solids' accretion can be of a similar order of magnitude to the contraction luminosity.

Keywords: accretion, accretion disks — hydrodynamics — methods: numerical — planet-disk interactions — planets and satellites: formation — protoplanetary disks

1. INTRODUCTION

Planetesimal accretion is a key process in the formation of a giant planet. In the Core-Nucleated Accretion (CNA) scenario (Pollack et al. 1996), planetesimal accretion accounts for the formation of the initial core (Phase 1). Additional planetesimal capture during the slow accretion of the gaseous envelope (Phase 2) releases gravitational energy, which must be radiated so that the envelope can contract. As the captured planetesimals pass through the envelope and ablate, they leave behind solid grains which affect the opacity. Both the energy release by sinking solids and the opacity affect the planet luminosity and help determine the duration of Phase 2 (Hubickyj et al. 2005; Movshovitz & Podolak 2008; Movshovitz et al. 2010). This ablated material will also affect the subsequent composition in the envelope (Iaroslavitz & Podolak 2007; Mousis et al. 2014). After the rapid gas accretion and ensuing contraction (Phase 3), when the planet has acquired most of its mass, additional accretion of solids occurs both onto the planet and in the subdisk surrounding the planet (the circumplanetary disk). This additional accretion adds relatively little to the planet itself, but can have important consequences for the formation of the regular satellites (e.g., Canup & Ward 2009; Estrada et al. 2009) and, possibly, for the occurrence of the irregular satellites.

As computing power has increased, studies of planetesimal accretion have become more detailed. Pollack et al. (1996) calculated the accretion rate assuming that the planetesimals were uniformly distributed over the feeding zone. Inaba et al. (2003) used a statistical model, which simulated such effects as scattering and collisions between planetesimals. Modifications and improvements of this idea have been employed over the past few years (Kobayashi et al. 2010; Bromley & Kenyon 2011). More recently, D'Angelo et al. (2014) revisited the problem combining detailed calculations for the evolution of a swarm of planetesimals and for the structure of the planet's envelope, up to the beginning of Phase 2.

The last stage of accretion, after the planet has undergone its rapid contraction, presents special difficulties. The planet is massive enough to open a gap in the gas density distribution of the circumstellar disk, and this constrains the motion of the gas flowing toward the planet (e.g., Lissauer et al. 2009, and references therein). The inflowing gas and the associated circumplanetary disk, in turn, affect how planetesimals are delivered to and captured by the subdisk and by the planet itself. Additionally, planet-induced perturbations on the gas may impact the redistribution of planetesimals in the circumstellar disk. In this work, we present the results of calculations that combine the three-dimensional (3D) gas dynamics with an N-body module to study these processes in detail, including the determination of temperature, ablation, and fragmentation of planetesimals. We consider the case of a giant planet of one Jupiter's mass and model solids in the (initial) size range 0.1–100 km. Results are presented also for smaller bodies, down to

¹ NASA Ames Research Center, MS 245-3, Moffett Field, CA 94035, USA (gennaro.dangelo@nasa.gov)

² SETI Institute, 189 Bernardo Avenue, Mountain View, CA 94043, USA

³ Department of Geosciences, Tel Aviv University, Ramat Aviv 69978, Israel (morris@post.tau.ac.il)

Table 1
List of Symbols

Symbol	Definition
$\{r, \theta, \phi\}$	Stellocentric spherical polar coordinates
$r_{\text{mn}, \text{mx}}$	Min/Max grid radius
$\theta_{\text{mn}, \text{mx}}$	Min/Max grid co-latitude angle
M_\star	Stellar mass
Ω_f	Frame rotation rate
Ω_p	Planet rotation rate
M_p	Planet mass
R_p	Planet radius
R_H	Planet's Hill radius
a_p	Planet semi-major axis
\mathbf{r}_p	Planet position
\mathbf{v}_g	Gas velocity
ρ_g	Gas volume density
Σ_g	Gas surface density
P_g	Gas pressure
c_g	Gas sound speed
ν_g	Turbulence kinematic viscosity
α_g	Turbulence viscosity parameter
$\{\rho_0, \Sigma_0\}$	Circumstellar disk reference densities
H	Circumstellar disk pressure scale-height
T_n	Circumstellar disk temperature
T_g	Gas temperature
μ_g	Gas mean molecular weight
η_g	Gas molecular dynamical viscosity
$\{L_r, L_\theta, L_\phi\}$	Particle specific linear/angular momenta
$\{\mathbf{r}_s, \mathbf{v}_s, \mathbf{a}_s\}$	Particle position, velocity, and acceleration
$\{\mathbf{F}_D, \mathbf{a}_D\}$	Aerodynamic drag force and acceleration
C_D	Drag coefficient
\mathcal{M}	Mach number
\mathcal{R}	Reynolds number
\mathcal{B}	Biot number
ρ_s	Particle density
M_s	Particle mass
R_s	Particle radius
ϵ_s	Particle emissivity
L_s	Particle specific vaporization energy
C_s	Particle specific heat
T_s	Particle temperature
λ_s	Particle thermal conductivity
δ_s	Particle isothermal depth
μ_s	Particle mean molecular weight
σ_s	Nominal material compressive strength
P_v	Particle vapor pressure
T_{cr}	Particle critical temperature
P_{dy}	Dynamical pressure
R_{dy}	Particle break-up radius
Ψ	Rock volume fraction of mixed medium
$\{\Phi_l, \Phi_u\}$	Conductivity efficiency factors of mixed medium
$\{x, y, z\}$	Planetocentric cartesian coordinates
\tilde{r}	Distance from the planet
T_e	Circumplanetary disk effective temperature
H	Circumplanetary disk local thickness
κ_R	Rosseland mean opacity

1 cm in radius.

In what follows, we describe how the thermodynamical evolution of the disk's gas and of the solids is calculated in Sections 2 and 3, respectively. The numerical procedures are outlined in Section 4. Results for the disk evolution are presented in Section 5, and those for the evolution of planetesimals are presented in Sections 6 and 7. We conclude discussing our findings in Section 8. Finally, further details and numerical tests are given in Appendix A and B.

2. THERMODYNAMICAL EVOLUTION OF THE DISK

We work in a reference frame whose origin is fixed to the star and which rotates about the origin at a rate Ω_f ,

equal to the angular velocity of the planet around the star, Ω_p . For a planet on a circular orbit, Ω_p is equal to the mean-motion:

$$\Omega_p = \sqrt{\frac{G(M_\star + M_p)}{a_p^3}}, \quad (1)$$

where M_\star and M_p are the star's and planet's mass, respectively, and a_p is the planet's semi-major axis. The planet-to-star mass ratio is $M_p/M_\star = 9.8 \times 10^{-4}$. Table 1 contains a list of the main symbols used in this paper.

The circumstellar disk is represented by a spherical sector with an inner hole. Consider a spherical polar coordinate system $\{\mathcal{O}; r, \theta, \phi\}$, where r indicates the polar distance from the origin, \mathcal{O} , the angle θ is the co-latitude ($\theta = 0$ is the north pole, $\theta = \pi/2$ is the mid-plane, and $\pi/2 - \theta$ is the latitude), and the angle ϕ is the azimuth. The disk volume is within the range given by $[r_{\text{mn}}, r_{\text{mx}}] \times [\theta_{\text{mn}}, \theta_{\text{mx}}] \times 2\pi$, where $r_{\text{mn}} = 0.4 a_p$ and $r_{\text{mx}} = 4 a_p$. We assume that the planet's orbit lies in the disk's equatorial plane, $\theta = \pi/2$, and that the disk is symmetric with respect to this plane. Consequently, only half of the disk volume needs to be simulated. Therefore, we set $\theta_{\text{mn}} \simeq 2\pi/5$ and $\theta_{\text{mx}} = \pi/2$.

The disk's gas is approximated to a viscous fluid of constant kinematic viscosity ν_g , volume density ρ_g , and velocity \mathbf{v}_g . In the following, all gas-related quantities will bear the subscript 'g'. The viscosity ν_g is typically assumed to arise from turbulence (of unspecified origin) within the gas, and needs not to be confused with the molecular viscosity, introduced below, which is much smaller in magnitude. We set $\nu_g = 10^{-5} a_p^2 \Omega_p$, which corresponds to a turbulence parameter (Shakura & Syun'yaev 1973) $\alpha_g = 0.004$ for our choice of the disk thickness.

We generally assume that the circumstellar gas is locally isothermal (the temperature depends only on r) and that the pressure is

$$P_g = c_g^2 \rho_g. \quad (2)$$

The gas sound speed is $c_g = (H/r)v_K$, and v_K is the local Keplerian velocity. The relative thickness of the disk above the equatorial plane, H/r , is taken to be constant and equal to 0.05. Therefore, the simulated disk volume extends in the vertical direction for more than 5.2 scale-heights, H . By assuming the equation of state for an ideal gas, the temperature in the circumstellar disk becomes

$$T_n = \left(\frac{\mu_g m_H}{k_B} \right) c_g^2, \quad (3)$$

where μ_g is the mean molecular weight of the gas, m_H is the hydrogen mass, and k_B is the Boltzmann constant. Since $c_g^2 \propto 1/r$, the gas temperature in the circumstellar disk is proportional to $1/r$ as well.

Given the thermal state of the gas, the disk region in which the gravity of the planet dominates over that of the star has a linear size on the order of the Hill radius, $R_H = a_p [M_p/(3M_\star)]^{1/3}$, which strictly speaking represents the distance of the Lagrange point L_1 from the planet (to leading order in M_p/M_\star , e.g., Kopal 1978; Murray & Dermott 2000). In absence of gas (i.e., neglecting pressure and viscosity effects), this region is a solid

Table 2
Disk's Gas Constants

H/r	ν_g^a	μ_g	γ_g	Σ_0^b	ρ_0^b
0.05	10^{-5}	2.39	1.4	10–100	10^{-12} – 10^{-11}

^a In units of $a_p^2 \Omega_p$.

^b Unperturbed Σ_g and ρ_g , in cgs units, at 5.2 AU.

of revolution (around the planet-star axis) whose volume is only about a third of that occupied by the Hill sphere. Thus, the effective (volumetric mean) radius of the region is $\approx 2R_H/3$ (Kopal 1959; Paczyński 1971; Kopal 1978; Eggleton 1983).

Table 2 summarizes the disk's gas parameters, assuming $M_\star = M_\odot$. The disk's reference densities at 5.2 AU are derived from evolution models discussed in Section 5. The mid-plane temperature of the disk at 5.2 AU, for the choice of parameters in Table 2, is ≈ 120 K. As explained in Section 5.1, the gas temperature distribution is given by Equation (3) but, in the restricted region of the circumplanetary disk, it is modified according to simple arguments based on local viscous heating, black-body heating by background radiation, and radiative cooling.

Orbital migration of the planet is neglected. At the higher Σ_0 considered here, the planet would drift inward at a speed $\sim \nu_g/a_p$ (D'Angelo & Lubow 2008). At the lower Σ_0 , migration would be inertia-limited and slower.

3. THERMODYNAMICAL EVOLUTION OF PLANETESIMALS

Here we describe the physical model for the thermodynamical evolution of the planetesimals. Since the model generally applies to any solid particle, regardless of the size, in this section we shall refer to the planetesimals simply as particles. All particle-related quantities will bear the subscript 's'. Sometimes, for ease of notation, this subscript is dropped.

3.1. Particle Dynamics

Let us introduce the linear momentum per unit mass in the radial direction $L_r = v_r$, the meridional angular momentum per unit mass $L_\theta = rv_\theta$, and the azimuthal angular momentum per unit mass $L_\phi = r \sin \theta v_\phi^A$, all defined in an inertial frame of reference. The velocity v_ϕ^A is the absolute azimuthal velocity: $v_\phi^A = v_\phi + (r \sin \theta)^2 \Omega_f$. In terms of these momenta, the equations of motion of a particle can be written as

$$\frac{dL_r}{dt} = a_r + \frac{1}{r} \left[\left(\frac{L_\theta}{r} \right)^2 + \left(\frac{L_\phi}{r \sin \theta} \right)^2 \right] \quad (4)$$

$$\frac{dL_\theta}{dt} = a_\theta r + \frac{\cos \theta}{\sin \theta} \left(\frac{L_\phi}{r \sin \theta} \right)^2 \quad (5)$$

$$\frac{dL_\phi}{dt} = a_\phi r \sin \theta, \quad (6)$$

where a_r , a_θ , and a_ϕ are the spherical components of the gravitational acceleration imparted to the particle. Notice that the subscript 's' associated to the coordinates and momenta of the particle is dropped.

In our case, the acceleration in Equations (4), (5), and (6) arises from the gravitational forces exerted by the

star and the planet, from non-inertial forces, and from the drag force exerted by the gas

$$\begin{aligned} \mathbf{a}_s = & \frac{GM_p(\mathbf{r}_p - \mathbf{r}_s)}{|\mathbf{r}_p - \mathbf{r}_s|^3} - \frac{GM_\star}{|\mathbf{r}_s|^3} \mathbf{r}_s + \mathbf{a}_D \\ & - \frac{GM_p}{|\mathbf{r}_p|^3} \mathbf{r}_p - \frac{GM_s}{|\mathbf{r}_s|^3} \mathbf{r}_s \\ & - \Omega_f \times (\Omega_f \times \mathbf{r}_s) - 2 \Omega_f \times \mathbf{v}_s \end{aligned} \quad (7)$$

where \mathbf{r}_p is the position vector of the planet, \mathbf{r}_s , \mathbf{v}_s , and M_s are position, velocity, and mass of the particle. The rotation rate vector, Ω_f , is parallel to the direction of the north pole ($\theta = 0$), i.e., $\Omega_f = \Omega_f \hat{\mathbf{z}}$. The components a_r , a_θ , and a_ϕ are found by projecting \mathbf{a}_s along the spherical polar unit vectors.

In Equation (7), the third term on the right-hand side, \mathbf{a}_D , is the drag acceleration. The fourth and fifth terms are the non-inertial accelerations imparted to the star (the origin) by the planet and the particle, respectively. The last two terms are the centrifugal and Coriolis accelerations. Additional terms may be included, such as the gravitational force per unit mass exerted by the disk on the particle, which we ignore here, and that exerted on the star, another non-inertial term, which is ignored as well.

Notice that Equations (4), (5), and (6) use absolute linear and angular momenta, hence they apply regardless of whether the vector Ω_f is constant or not. Equation (7) is valid for $\dot{\Omega}_f = \mathbf{0}$ and requires the additional non-inertial term $-\dot{\Omega}_f \times \mathbf{r}_s$ in case $\dot{\Omega}_f \neq \mathbf{0}$.

Let us indicate with A_s the cross section of a particle, then the drag force experienced by the particle while moving through the gas is

$$\mathbf{F}_D = \frac{1}{2} C_D A_s \rho_g |\mathbf{v}_g - \mathbf{v}_s| (\mathbf{v}_g - \mathbf{v}_s), \quad (8)$$

where C_D is the drag coefficient. For spherical particles of uniform density ρ_s and radius R_s , the drag force per unit mass becomes

$$\mathbf{a}_D = \frac{3}{8} \frac{C_D}{R_s} \left(\frac{\rho_g}{\rho_s} \right) |\mathbf{v}_g - \mathbf{v}_s| (\mathbf{v}_g - \mathbf{v}_s). \quad (9)$$

In general, the drag coefficient, C_D , depends on the (relative) Mach number

$$\mathcal{M} = \frac{|\mathbf{v}_g - \mathbf{v}_s|}{c_g}, \quad (10)$$

and on the (relative) Reynolds number, which can be written as

$$\mathcal{R} = 2R_s \rho_g \frac{|\mathbf{v}_g - \mathbf{v}_s|}{\eta_g}, \quad (11)$$

in which η_g represents the molecular dynamical viscosity of the gas. We use the expression for C_D derived by Melosh & Goldin (2008), which is a continuous function applicable over the full range of \mathcal{M} and \mathcal{R} . In the continuum flow limit, that occurs when $\mathcal{M}/\mathcal{R} \ll 1$, we embed in the coefficient of Melosh & Goldin (2008) a drag formula proposed by Brown & Lawler (2003). The drag coefficient is discussed in more detail in Appendix A.

3.2. Particle Thermodynamics

A particle moving through gas sweeps a mass per unit time equal to $A_g \rho_g |\mathbf{v}_g - \mathbf{v}_s|$. Collisions between gas atoms (and/or molecules) and the particle transfer some amount of the specific kinetic energy of the gas, $|\mathbf{v}_g - \mathbf{v}_s|^2/2$, to the particle at a rate $(f_{\text{EK}}/2)A_g \rho_g |\mathbf{v}_g - \mathbf{v}_s|^3$, where f_{EK} is the fraction of the total collisional kinetic energy transmitted as heat to the particle. This energy exchange can also be interpreted in terms of the rate at which work is done on the particle by drag in the gas frame $\mathbf{F}_D \cdot (\mathbf{v}_g - \mathbf{v}_s) = (C_D/2)A_s \rho_g |\mathbf{v}_g - \mathbf{v}_s|^3$, hence $f_{\text{EK}} \propto C_D$ with a proportionality factor ≤ 1 . Podolak et al. 1988 (hereafter PPR88) argued that an upper limit to the proportionality factor is $1/4$, though they discussed the possibility for it to be smaller. Here we take this upper limit and assume that $f_{\text{EK}} = C_D/4$. Therefore, the rate at which the particle gains energy due to frictional heating with the gas is $(\pi/8)C_D \rho_g R_s^2 |\mathbf{v}_g - \mathbf{v}_s|^3$.

Another source of heating is represented by the energy absorbed from the radiation emitted by the ambient gas at temperature T_g , $4\pi R_s^2 \epsilon_s \sigma_{\text{SB}} T_g^4$ (assuming black-body emission), where ϵ_s is the thermal emissivity of the particle (here assumed a perfect black-body radiator, $\epsilon_s = 1$ ⁴) and σ_{SB} is the Stefan-Boltzmann constant. Similarly, energy is lost via radiation emitted through the particle surface, $4\pi R_s^2 \epsilon_s \sigma_{\text{SB}} T_s^4$. Loosely speaking, T_s represents the particle temperature. More precisely, as we clarify below, it is the temperature of an outer isothermal layer of the particle.

Finally, there is energy involved in the phase transition of the particle's material. If dM_s/dt is the rate of change of the particle's mass and all of dM_s is involved in the phase transition, $L_s dM_s/dt$ is the energy per unit time absorbed (or released, depending on the sign of dM_s/dt) in the process, where L_s is the energy per unit mass required to vaporize the substance.

Accounting for all heating and cooling sources presented above, the energy balance equation takes the form

$$\begin{aligned} \frac{4}{3}\pi R_s^3 \rho_s C_s \frac{dT_s}{dt} &= \frac{\pi}{8} C_D \rho_g R_s^2 |\mathbf{v}_g - \mathbf{v}_s|^3 \\ &+ 4\pi R_s^2 \epsilon_s \sigma_{\text{SB}} (T_g^4 - T_s^4) \\ &+ L_s \frac{dM_s}{dt}. \end{aligned} \quad (12)$$

In Equation (12), C_s is the specific heat of the particle. Whipple (1950) estimated that, for typical meteoritic material, the the left-hand side may be ignored for particles smaller than the 0.01 cm in radius.

In Equation (12), the variation of the particle's internal energy (the left-hand side), assumes that the temperature T_s is uniform throughout the volume of the body. Such assumption requires that there be no temperature gradient inside the body, i.e., that internal heat conduction be infinite. This may indeed be the case for small particles but, as the particle radius increases, the presence of a temperature gradient within the body becomes increasingly non-negligible. For example, Love & Brownlee (1991) concluded that a significant temperature gradient may begin to appear across particles with a diam-

eter larger than ~ 0.1 cm when $T_s \approx 1500$ K. Therefore, the isothermality assumption advocated in Equation (12) may be justified only in an outer shell of the body.

In order to evaluate the thickness of the surface layer of a particle, which may be approximated as isothermal at temperature T_s , we follow the approach of McAuliffe & Christou (2006), based on the work of Love & Brownlee (1991). A measure of whether or not a temperature gradient develops inside a heated body can be derived from the Biot number, which is defined as

$$\mathcal{B} \equiv \frac{h_c l_c}{\lambda_s}, \quad (13)$$

where h_c is a characteristic heat transfer coefficient, with the units of an energy flux per unit temperature, l_c is a characteristic length, and λ_s is the thermal conductivity of the material. The quantity h_c is intended to represent the rate of heat exchange between the body and the surrounding environment, as a function of the difference of temperature between them. The characteristic length l_c is typically defined as the volume-to-surface ratio. For a sphere, l_c is a third of the radius.

It is customary to assume that temperature gradients inside a given substance are negligible for $\mathcal{B} \leq 0.1$ (e.g., Lienhard & Lienhard 2008). Love & Brownlee (1991) approximated the characteristic heat transfer coefficient h_c of a layer at temperature T_s as $\sigma_{\text{SB}} T_s^3$. Thus, from Equation (13), one can approximate the maximum thickness of the isothermal layer δ_s to

$$\delta_s = 0.3 \left(\frac{\lambda_s}{\sigma_{\text{SB}} T_s^3} \right). \quad (14)$$

Obviously, δ_s has an upper bound at R_s , in which case the body can be considered as fully isothermal.

Therefore, in general, we will assume that heating and cooling processes affect only a surface layer of the body, of thickness δ_s , rather than its entire volume. In this approximation, Equation (12) can be re-written as

$$\begin{aligned} \frac{4}{3}\pi [R_s^3 - (R_s - \delta_s)^3] \rho_s C_s \frac{dT_s}{dt} &= \frac{\pi}{8} C_D \rho_g R_s^2 |\mathbf{v}_g - \mathbf{v}_s|^3 \\ &+ 4\pi R_s^2 \epsilon_s \sigma_{\text{SB}} (T_g^4 - T_s^4) \\ &+ L_s \frac{dM_s}{dt}. \end{aligned} \quad (15)$$

Note that, in the above equation, the particle radius may vary with time due to ablation. At $T_s = 100$ K, the maximum isothermal depth, δ_s , of an icy particle is few tens of meters, and somewhat less than ten meters at 150 K. Since λ_s varies by a factor less than 2 between the two temperatures (see Table 3), this change in δ_s is mainly dictated by the increased heat exchange with the surroundings. The quoted depths become larger for rocky (quartz) bodies by a factor of ≈ 3 (see Table 3), but they are broadly in accord with the estimate of PPR88, who concluded that heating and cooling would affect only a relatively thin layer of large, km-size bodies. This approach, however, is rendered necessary by the fact that planetesimals may spend most of their time in the cool circumstellar and circumplanetary disk environments.

In Equations (14) and (15), both the thermal conduc-

⁴ This is a very good approximation for ice (and water), and typically a reasonable approximation for silicates.

Table 3
Material's Properties

Symbol	Ice	Rock	Ice+Rock
ρ_s^a [g cm ⁻³]	1.00	2.65	1.33
ε_s^b	1.00	1.00	1.00
L_s^c [erg g ⁻¹]	2.83×10^{10}	8.08×10^{10}	2.83×10^{10}
L_s^d [erg g ⁻¹]	2.50×10^{10}	7.92×10^{10}	2.50×10^{10}
μ_s^e	18.0	60.1	25.0
σ_s^f [dyne cm ⁻²]	10^6	10^7	10^6
C_s^g [erg g ⁻¹ K ⁻¹]			
at 50 K	4.35×10^6	9.56×10^5	2.99×10^6
at 100 K	8.30×10^6	2.67×10^6	6.05×10^6
at 200 K	1.58×10^7	5.43×10^6	1.17×10^7
λ_s^h [erg s ⁻¹ cm ⁻¹ K ⁻¹]			
at 50 K	1.33×10^6	5.89×10^6	1.85×10^6
at 100 K	6.41×10^5	2.09×10^6	8.33×10^5
at 200 K	3.10×10^5	9.55×10^5	3.98×10^5

^a Density.

^b Thermal emissivity.

^c Specific vaporization energy of the solid phase.

^d Specific vaporization energy of the liquid phase.

^e Mean molecular weight.

^f Nominal compressive strength at $R_s = 10^5$ cm.

^g Specific heat.

^h Thermal conductivity.

tivity λ_s and the specific heat C_s are functions of T_s ⁵. We use piece-wise fits to the data reported by Haynes (2011) and Jensen et al. (1980) for ice and by Powell et al. (1966) and Chase (1998) for quartz (SiO₂). The specific energy of vaporization, L_s , is instead approximated as constant (see discussion in PPR88). Here, rather than rocks, we consider a mixture in which rocks are embedded in an icy matrix. Indicating the mass fractions of ice and rock with χ_{ice} and χ_{rock} (so that $\chi_{\text{ice}} + \chi_{\text{rock}} = 1$), the specific heat of the mixture is given by

$$C_s = \chi_{\text{ice}} C_s^{\text{ice}} + \chi_{\text{rock}} C_s^{\text{rock}}. \quad (16)$$

The thermal conductivity of the mixture is approximated as

$$\lambda_s = \lambda_s^{\text{ice}} [(1 - \Psi)\Phi_u + \Psi\Phi_l], \quad (17)$$

where $\Psi = \chi_{\text{rock}} \rho_s^{\text{ice}} / (\chi_{\text{rock}} \rho_s^{\text{ice}} + \chi_{\text{ice}} \rho_s^{\text{rock}})$ is the fraction of the volume occupied by rock. The quantities Φ_u and Φ_l represent efficiency factors for the thermal conductivity of a mixed medium, composed of a matrix of one material embedding grains of a second material (see discussion in Prialnik et al. 2004). Rock would constitute the matrix of the mixed medium for $\Psi > 0.5$. In Equation (17), Φ_u and Φ_l are both functions of Ψ and $\lambda_s^{\text{rock}}/\lambda_s^{\text{ice}}$, and are respectively given by Equations (25) and (26) of Prialnik et al. (2004). Equation (17) converges to λ_s^{ice} for $\Psi \rightarrow 0$ (both Φ_u and $\Phi_l \rightarrow 1$) and to λ_s^{rock} for $\Psi \rightarrow 1$ (both Φ_u and $\Phi_l \rightarrow \lambda_s^{\text{rock}}/\lambda_s^{\text{ice}}$). We use an ice mass fraction $\chi_{\text{ice}} = 0.6$, hence $\Psi \simeq 0.334$. The medium remains mixed throughout the evolution and possible effects of differentiation (Mosqueira et al. 2010) are ignored. A summary of some material's properties is listed in Table 3, including values of C_s and λ_s at three representative temperatures.

⁵ Here, the material is assumed to be compact, and possible effects due porosity, inhomogeneity and impurity of the substance are neglected.

3.3. Particle Ablation

The heat deposited in the outer layer of a body can cause phase transitions of its material, and hence mass loss. Here we consider that mass loss is caused by transition to the gas phase. The rate at which vaporization removes mass from a solid body can be approximated by the Hertz-Knudsen-Langmuir equation (e.g., Blottner 1971; Campbell-Brown & Koschny 2004, and references therein). Indicating with P_v and μ_s , respectively, the vapor pressure and the mean molecular weight of the material, arguments from the kinetic theory of gases imply that the flux of atoms/molecules leaving the surface of a body is $\mu_s m_H P_v / (k_B T_s) \bar{V}_s / 4$, where \bar{V}_s is the average thermal speed of atoms/molecules in the vapor (e.g., Mihalas & Weibel Mihalas 1999):

$$\bar{V}_s = \sqrt{\frac{8}{\pi} \frac{k_B T_s}{\mu_s m_H}}. \quad (18)$$

Integrating the flux over the surface of the (spherical) body, we have that the mass loss rate is

$$\frac{dM_s}{dt} = -4\pi R_s^2 P_v \sqrt{\frac{\mu_s m_H}{2\pi k_B T_s}}, \quad (19)$$

and $P_v = P_v(T_s)$. Equation (19) assumes that the vapor is rapidly carried away from the body's surface, i.e., the partial pressure of the vapor in the gas is unimportant. In case of the ice-rock mixture, vapor carries away the icy matrix first (due to higher vapor pressure), but we assume that the rocky material embedded in the matrix is also lost by appropriately modifying μ_s .

The vapor pressure can be obtained by integrating the Clausius-Clapeyron equation. The resulting function depends on a number of constants that are fixed using physical arguments and experimental data. For icy bodies, at temperatures below the melting point ($T_s = 273.16$ K), we use the formula of Washburn (1924), which reads

$$\log P_v = a_0 + a_1 T_s + a_2 T_s^2 + \frac{a_3}{T_s} + a_4 \log T_s. \quad (20)$$

For P_v expressed in units of dyne/cm² (= 0.1 Pa), the constants a_i are given in Table 4. Although Washburn's formula dates back 90 years, it agrees very well with the 2011 release of the sublimation pressure of ordinary water ice from The International Association for the Properties of Water and Steam. Washburn (1924) found that Equation (20) satisfactorily reproduced the experimental data accessible to him (above ~ 170 K). We find that this formula actually gives a good fit to all the values of the vapor pressure of ice reported by Haynes (2011), which extend down to 50 K.

Above the melting point and below the critical temperature, $T_{\text{cr}} = 647.096$ K, we use the fitting function from Wagner & Pruß (2002)

$$\ln\left(\frac{P_v}{P_{\text{cr}}}\right) = \left(\frac{T_{\text{cr}}}{T_s}\right) (a_0 \vartheta_s + a_1 \vartheta_s^{1.5} + a_2 \vartheta_s^3 + a_3 \vartheta_s^{3.5} + a_4 \vartheta_s^4 + a_5 \vartheta_s^{7.5}), \quad (21)$$

where $\vartheta_s = (1 - T_s/T_{\text{cr}})$, $P_{\text{cr}} = 2.2064 \times 10^8$ dyne/cm² is the vapor pressure at the critical temperature, and the constants a_i can be found in Table 4. We find that the

Table 4
Constants in Vapor Pressure Formulas^a

Equation	a_0	a_1	a_2	a_3	a_4	a_5
(20)	-2445.5646	8.2312	-0.01677006	0.0000120514	-3.632266	
(21)	-7.85951783	1.84408259	-11.7866497	22.6807411	-15.9618719	1.80122502
(22)	31.82319964	46071.4304	58.883			

^a The pressure is in units of dyne/cm².

vapor pressure from Equation (21) becomes larger than that from Equation (20) for $T_s > 272.84$ K, hence we use this temperature value for the transition between the two formulas, Equations (20) and (21).

Alternatively, the vapor pressure can be derived by fitting experimental data. For quartz, we adopt the fitting function published on the Chemistry WebBook of the National Institute of Standards and Technology (NIST)

$$\ln P_v = a_0 - \frac{a_1}{T_s + a_2}. \quad (22)$$

The constants a_i are displayed in Table 4 for P_v expressed in units of dyne/cm². This NIST fit applies over a limited range of temperatures, and it should be considered as an extrapolation at lower temperatures and up to the critical temperature, $T_{cr} = 4500$ K. However, since the vapor pressure of the icy matrix is much higher, the mass loss of mixed-composition particles is also governed by Equations (20) and (21).

At temperatures greater than T_{cr} , there is no distinction between the vapor and the liquid phase and the mass loss rate is energy limited (see PPR88). For $T_s \geq T_{cr}$, the mass vaporization rate is

$$\frac{dM_s}{dt} = \frac{1}{L_s} \left[4\pi R_s^2 \epsilon_s \sigma_{SB} (T_{cr}^4 - T_g^4) - \frac{\pi}{8} C_D \rho_g R_s^2 |\mathbf{v}_g - \mathbf{v}_s|^3 \right]. \quad (23)$$

When $T_s = T_{cr}$, a particle evaporates at a constant temperature (Hood & Horanyi 1991). At and beyond the critical temperature, any net energy input is used for ablation. If there is a net energy output (i.e., when radiative cooling becomes larger than the sum of frictional and radiative heating) the vaporization rate is set to zero.

Equations (19) and (23) are applied together with the Equations of motion (4), (5), and (6) under the hypothesis of isotropic mass loss, where the isotropy is with respect to the center of mass of the moving body. In other words, it is assumed that the absolute momenta of the escaping mass are equal to those said mass would have if it was attached to the moving body (Kopal 1978).

3.4. Fracturing and Break-up of Planetesimals

A solid body acted upon by external forces is stressed to some degree. In case of a spherical body, if the stress overcomes the compressive strength of the material, the body can fracture. Pollack et al. (1979) (see also Baldwin & Sheaffer 1971) approximated the differential force (per unit surface area) across a body traveling through gas as the dynamical pressure

$$P_{dy} = \frac{1}{2} \rho_g |\mathbf{v}_g - \mathbf{v}_s|^2. \quad (24)$$

Non-spherical bodies are also subject to bending, hence they can fracture at stresses lower by about an order of magnitude, i.e., once the tensile strength is exceeded (see discussion in Baldwin & Sheaffer 1971). The compressive strength has typically an inverse dependence on the body size, the body temperature, and the material porosity (Petrovic 2003). Material strengths are also sensitive to the rate of strain (e.g., Lange & Ahrens 1983), i.e., the rate at which the external force is applied. This may be especially important for large bodies. Simulations and laboratory experiments suggest that the strength of rocky, iron, and icy bodies is proportional to $1/R_s$ to a some power, which is typically between 0.3 and 0.5 (Housen & Holsapple 1999; Benz & Asphaug 1999).

A fractured body can quickly break apart, unless it is held together by its own gravity, which occurs if the radius exceeds

$$R_{dy} = \sqrt{\frac{5}{4\pi} \frac{P_{dy}}{G\rho_s^2}}. \quad (25)$$

(Pollack et al. 1979, 1986). Here we assume that if $R_s < R_{dy}$ and the dynamical pressure exceeds the compressive strength of the particle's material, the body is completely disrupted and the fragments quickly dissolve (which is probably a good approximation if the fragments are sufficiently small). If $R_s > R_{dy}$ the body *does not* break apart, independently of P_{dy} .

The compressive strengths of planetesimals are largely unknown. Data obtained from the fragmentation of stony and iron meteorites in the Earth's atmosphere imply strengths within the range from 10^6 to 10^9 dyne/cm² (Cepelcha 1993; Petrovic 2001; Popova et al. 2011). The compressive strength of solid ice is on the order of 10^7 dyne/cm² (Petrovic 2003), though it is expected to be lower for porous ice (Cox & Richter-Menge 1985). The inferred compressive strength of primitive icy bodies in the solar system, such as comets, is much smaller, $\lesssim 10^4$ dyne/cm² (Toth & Lisse 2006). PPR88 argued that the old age of comets may have significantly altered their mechanical properties through outgassing. Biele et al. (2009) also pointed out that strengths measured from comets may be affected by pre-existing faulting. Thus, the compressive strength of "young" icy planetesimals may as well be in the range from $\sim 10^5$ to $\sim 10^6$ dyne/cm².

Given the large uncertainties, we set the material compressive strength to $\sigma_s \sqrt{1 \text{ km}/R_s}$ (Holsapple 2009). The nominal strength, σ_s , at the 1 km-scale size is 10^6 and 10^7 dyne/cm² for icy and rocky planetesimals, respectively (see Table 3). This choice of the compressive strengths implies that, according Equation (25), only icy (rocky) bodies whose radius is smaller than ≈ 10 km

Table 5
Grid Structure

Level	N_r	N_θ	N_ϕ	Volume ^a
1	243	22	423	disk
2	84	24	84	$9.13 \times 2.53 \times 9.15$
3	104	34	104	$5.65 \times 1.79 \times 5.66$
4	124	44	124	$3.37 \times 1.16 \times 3.37$
5	164	64	164	$2.23 \times 0.84 \times 2.23$
6	244	84	244	$1.66 \times 0.55 \times 1.66$
7	404	104	404	$1.37 \times 0.34 \times 1.37$
8	724	144	724	$1.23 \times 0.24 \times 1.23$

^a Volume is in units of R_H^3 , except for grid level 1.

(≈ 20 km) can fragment, if the dynamical pressure is just marginally larger than the compressive strength. Larger bodies can fracture more easily, but are held together by their own gravity. However, the maximum radius for break-up increases as P_{dy} increases.

4. NUMERICAL METHODS

4.1. Solution for the Disk Hydrodynamics

The disk's gas is described as a continuum viscous fluid via the Navier-Stokes equations (see, e.g., [Mihalas & Weibel Mihalas 1999](#)), written in terms of the specific linear momentum and the specific total angular momenta of the gas in a rotating frame (see [D'Angelo et al. 2005](#)). These equations are solved in a stepwise fashion by means of a finite-difference code. The solution of the advection term, referred to as the transport step, applies the monotonic transport of [van Leer \(1977\)](#) and uses an operator-splitting technique (see [Stone & Norman 1992](#)) to cope with the three dimensions. In the source step, the other terms of the equations are taken into account, namely the apparent forces, the gradients of pressure and gravity, and the viscous stresses. Numerical stability is ensured by constraining the integration time step, Δt , according to the Courant-Friedrichs-Lewy condition (see [Stone & Norman 1992](#)). Overall, the algorithm is second-order accurate in space and effectively second-order accurate in time (e.g., [Boss & Myhill 1992](#)). The code was compared against other fluid dynamics codes in studies involving problems of tidal interactions between planets and disks ([de Val-Borro et al. 2006](#); [Masset et al. 2006](#); [de Val-Borro et al. 2007](#)).

The Navier-Stokes momentum equations are discretized over a spherical polar grid with constant spacing in all three coordinate directions. The code allows for grid refinements by means of a nested-grid technique ([D'Angelo et al. 2002, 2003a](#)). The increase of volume resolution is a factor of 2^3 for any level added to the grid system. In this study, we employ a grid system with 8 levels, the details of which are given in Table 5. The first level encloses the entire disk, whereas additional levels enclose smaller and smaller disk portions around the planet. In Table 5, N_r , N_θ , and N_ϕ indicate the number of grid points along the correspondent coordinate directions. The last column gives the volume occupied by each grid level, where the lengths are in units of R_H . Overall, the grid system contains about 103 million grid elements. The region of the wider circumplanetary disk, typically taken as $\sim R_H/4$ around the planet, is discretized over the 8th grid with more than 12 million grid elements.

The spatial resolution on the first grid level is such that $\Delta r/a_p \simeq a_p \Delta\phi/(r \sin\theta) \simeq 0.015$ and $a_p \Delta\theta/r \simeq 0.013$. On the 8th grid level, the linear resolution around the planet is $\approx 10^{-4} a_p \approx 1.4 \times 10^{-3} R_H$, which is about equal to Jupiter's current radius, R_J , at 5.2 AU. Note that the actual radius of the planet, R_p , at these late stages of accretion (i.e., when it is no longer accreting substantial quantities of gas compared to its mass) is likely $\gtrsim 1.3 R_J$ and $\lesssim 1.8 R_J$ ([Lissauer et al. 2009](#)). We adopt the value $R_p = 1.6 R_J$.

We apply boundary conditions at the inner and outer disk radii, r_{mn} and r_{mx} , using the procedures of [de Val-Borro et al. \(2006\)](#). Boundaries at the disk surface ($\theta = \theta_{mn}$) and at the equatorial plane are handled as in [Masset et al. \(2006\)](#). In these calculations, we do not account for accretion on the central star which, in conjunction with accretion on the planet, can alter the density in the disk interior of the planet's orbit ([Lubow & D'Angelo 2006](#)).

4.2. Solution for the Planetesimal Thermodynamics

The set of Equations (4)–(6) is completed by the equations to obtain the spherical polar coordinates of a particle

$$\begin{aligned} \frac{dr}{dt} &= L_r \\ \frac{d\theta}{dt} &= \frac{L_\theta}{r^2} \\ \frac{d\phi}{dt} &= \frac{L_\phi}{(r \sin\theta)^2} - \Omega_f. \end{aligned} \quad (26)$$

The system of first order ordinary differential equations (ODE), represented by Equations (26), (4), (5), (6), (15), and (19) or (23), is solved numerically by means of a variable (arbitrarily high) order and variable step-size Gragg-Bulirsch-Stoer extrapolation algorithm ([Hairer et al. 1993](#)). Indicating with Δt the time step of the hydrodynamical calculation at time t (see Section 4.2), the system of ODE is integrated three times, according to the step-size sequence $(\Delta t/4, \Delta t/2, \Delta t/4)$, using gas field distributions centered at $(t, t+\Delta t/2, t+\Delta t)$, respectively.

The ODE solver chooses automatically the order of the algorithm and a series of appropriate internal time intervals so to advance the solution to the required end time. The algorithm's order and the length of each time interval are constrained by user-supplied tolerances on the local truncation error of the solution, which is estimated from the comparison of solutions at different orders. Here we apply tolerances in the range from 2×10^{-16} to 10^{-10} .

The 3D gas field distributions of ρ_g , T_g , and \mathbf{v}_g , are interpolated in space at the position of the particles by means of a second-order accurate algorithm, based on monotonic harmonic means ([van Leer 1977](#)), according to the approach of [D'Angelo et al. \(2002\)](#), extended to three dimensions. The advantage of this method rests on its capability of handling discontinuities and shock-like conditions in the gas. The spatial as well as temporal interpolations are performed on the gas field distributions with the highest available resolution, which are those calculated on the most refined grid level where the particle is located.

Several tests of the planetesimal thermodynamics solver are presented in Appendix B. These include standard two- and three-body problems, drag-induced orbital

decay and free-fall of particles, and various thermal evolution problems.

4.3. Gas and Particle Accretion

The accretion of gas onto a gap-opening planet is a complex problem. It was suggested by D'Angelo et al. (2003b) and Bate et al. (2003), and later confirmed (see the recent studies by Tanigawa et al. 2012; Ayliffe & Bate 2012; Gressel et al. 2013; Szulágyi et al. 2014, and references therein), that gas mostly proceeds off the mid-plane (at and above the surface) of the disk around the planet, prior to accreting on its envelope. We do not model the planet's envelope here and adopt a prescription for gas accretion along the lines of D'Angelo et al. (2003b) and D'Angelo & Lubow (2008), a procedure that is directionally unbiased. The spherical volume around the planet from which gas is removed to mimic accretion extends for $1.4 R_p$ in radius ($\approx 2.2 R_J$), which makes the procedure independent of the mode of gas delivery to the planet's envelope. At such short distances, the thermal energy of the gas is much smaller than the gravitational energy binding the gas to the planet (Bodenheimer & Pollack 1986), hence gas cannot escape. Planet formation calculations do indicate that the rates of accretion calculated in this manner correspond to the actual rates of envelope growth (Lissauer et al. 2009).

The accretion of planetesimals is a simpler problem, since arbitrarily close encounters with the planet are allowed. During close approaches, the gravitational potential of the planet is always used, and no regularization is applied (see, e.g., Bodenheimer et al. 2006). We adopt two criteria for accretion: if the particle approaches the planet within a distance $\leq R_p$ ($1.6 R_J$), a head-on impact is assumed; otherwise, and if the distance of approach is $\leq 2.2 R_p$ ($3.5 R_J$), the particle is deemed as accreted if its relative velocity is less than the escape velocity from the planet at that distance.

5. DISK DENSITY AND DYNAMICS

D'Angelo & Marzari (2012) performed calculations of circumstellar disk evolution driven by viscous diffusion and photoevaporation, exploring ranges of stellar EUV luminosity, initial disk mass, initial mass distribution, and gas kinematic viscosity representative of the proto-sun and the early solar nebula. These parameters can be constrained by the requirements that the disk's gas lifetime be shorter than 20 Myr (e.g., Haisch et al. 2001; Pascucci et al. 2006; Roberge & Kamp 2011; Williams & Cieza 2011; Bell et al. 2013) and longer than the formation time of a Jupiter-mass planet at ≈ 5 AU, which is $\gtrsim 1$ Myr (Hubickyj et al. 2005; Alibert et al. 2005; Lissauer et al. 2009; Movshovitz et al. 2010; Mordasini et al. 2011).

In Figure 1, we plot results from some models of D'Angelo & Marzari (2012), in particular the surface density at 5 AU versus time. The ratio of the initial disk mass to the stellar mass is indicated in the top-right corner. The curves indicate that, after ~ 1 Myr, the density is at most $\approx 200 \text{ g cm}^{-2}$, and is typically smaller than 100 g cm^{-2} (but could be much smaller, $\approx 20 \text{ g cm}^{-2}$). After ~ 2 Myr, the surface density ranges from ~ 10 to $\sim 50 \text{ g cm}^{-2}$. In all the models in the figure, the initial surface density inside of about 10 AU is proportional to

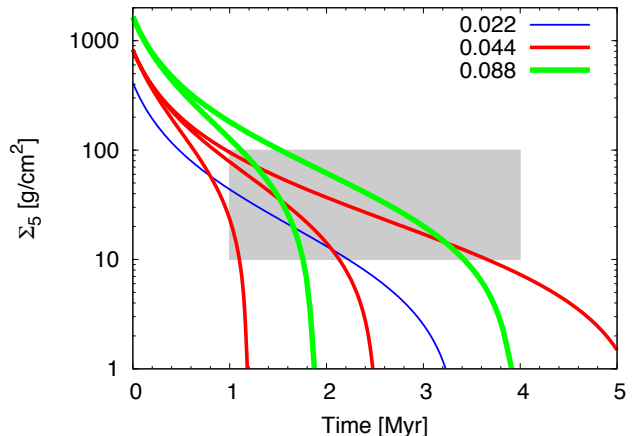


Figure 1. Surface density at 5 AU versus time in disk models whose evolution is driven by viscous diffusion and photoevaporation. The numbers in the legend indicate the initial disk mass, in units of M_* , within 40 AU of the star. The models also employ different gas kinematic viscosities and EUV fluxes emitted by the star. See text for an explanation of the shaded area. Data from the models of D'Angelo & Marzari (2012).

$1/\sqrt{r}$, consistent with that used in the hydrodynamical calculations.

Therefore, given the range of possible disk densities at the time of Jupiter's formation (between, say, ~ 1 and ~ 4 Myr), we consider two values for the unperturbed surface density, Σ_0 , at 5.2 AU of ≈ 10 and $\approx 100 \text{ g cm}^{-2}$, which correspond to mass densities $\rho_0 \approx 10^{-12}$ and $\rho_0 \approx 10^{-11} \text{ g cm}^{-3}$. The shaded area in Figure 1 represents the area covered by our choice of Σ_0 . The disk mass in units of M_* , inside of ≈ 21 AU, is $\approx 8 \times 10^{-5} \Sigma_0$, where Σ_0 is in units of g cm^{-2} .

Tidal interactions between the disk's gas and the planet excite density waves at Lindblad resonances (Goldreich & Tremaine 1980) and deplete the gas within a few R_H from the planet's orbit, where tidal torques exceed viscous torques (Lin & Papaloizou 1986). Residual gas is still present in the tidal gap region (as shown below), even at a viscosity much smaller than that adopted here.

The main features of the surface and volume density, on a global disk scale ($\gtrsim a_p$), are illustrated in Figure 2. In all cases, densities are normalized to either Σ_0 or ρ_0 . Both spiral density waves and the tidally-produced gap are visible in the top-left panel, while the plot on the right shows, more quantitatively, the volume density in the disk's equatorial plane, at several distances from the planet's orbit. The residual gas in the tidal gap region is also visible as a function of the azimuthal angle. The center panels illustrate the density on orthogonal disk slices passing through the planet's position, on different length scales. The surface density of the region around the planet's Roche lobe is shown in the bottom panels (the left panel also shows the Roche lobe trace and the positions of the Lagrange points L_1 – lower cross – and L_2 – upper cross). Radial cuts of Σ_g/Σ_0 at various azimuthal angles are plotted in the right panel. All images are saturated in order to improve the contrast between low and high density regions.

The rotation curve of the unperturbed disk is affected by the gas pressure gradient, which depends on both density and temperature gradients. In terms of the Keple-

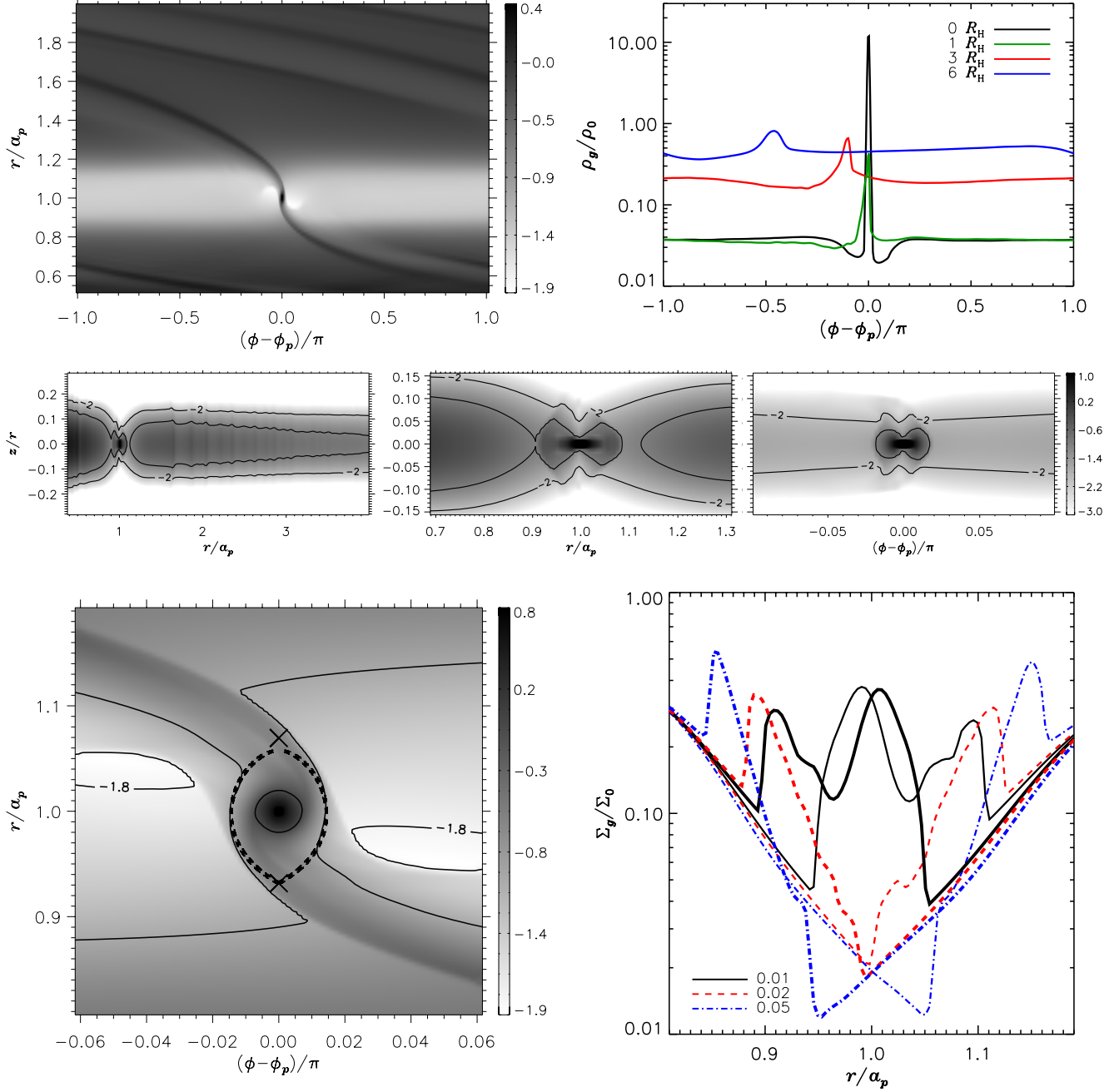


Figure 2. Top-left. Color scale rendering of $\log(\Sigma_g/\Sigma_0)$ as a function of the azimuthal angle from the planet and the distance from the star in units of a_p . Top-right. Volume density, ρ_g in the disk's mid-plane, normalized to ρ_0 as a function of the azimuth at various distances from the planet's orbit, as indicated in the legend. Center. Color scale rendering of $\log(\rho_g/\rho_0)$ on disk slices passing through the planet. The latitude ($\approx z/r$) is on the vertical axis and the linear distance from the star (left and middle) or angular distance from the planet (right) is on the horizontal axis. Bottom. Color scale rendering of $\log(\Sigma_g/\Sigma_0)$ in the proximity of the planet's Roche lobe (left) and Σ_g/Σ_0 versus radial distance (right), at various separation angles, $|\phi - \phi_p|/\pi$, as indicated. Thicker lines are for $\phi > \phi_p$.

rian velocity, v_K , the (absolute) azimuthal velocity of the gas, in absence of the planet and in the mid-plane of the disk, would be (e.g., Tanaka et al. 2002)

$$(v_\phi^A)_u = v_K \left[1 - \frac{5}{2} \left(\frac{H}{r} \right)^2 \right]^{1/2}, \quad (27)$$

which accounts for the fact that the unperturbed density

is $\rho_g \propto 1/r^{3/2}$ and $T_g \propto 1/r$. The subscript “u” stresses the fact that this expression does not account for the perturbation induced by the planet. Velocity $(v_\phi^A)_u$ differs by less than 1% from the Keplerian velocity. The ratio of the perturbed velocity, v_ϕ^A , to that in Equation (27) is shown in Figure 3. The largest deviations from the unperturbed rotation curve occur around the edges of the gap, where the magnitude of the density

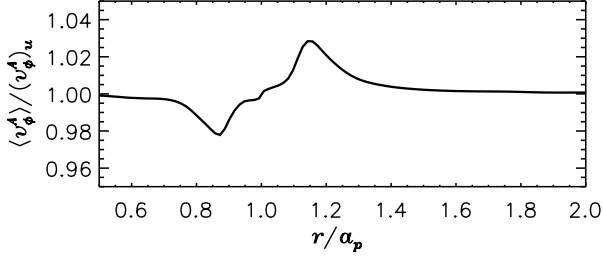


Figure 3. Absolute azimuthal velocity of the gas, averaged over 2π in azimuth around the star and normalized to the unperturbed velocity of Equation (27). The radial pressure gradient of the gas induces sub/super-Keplerian rotation at the inner/outer gap edge.

gradient is the largest (see top-left panel in Figure 2). The negative/positive pressure (radial) gradient triggers a sub/super-Keplerian rotation around the inner/outer edge of the gap. In fact, centrifugal balance requires that $(v_\phi^A)^2 = v_K^2 + (r/\rho_g)\partial P_g/\partial r$ or, using Equation (2),

$$v_\phi^A = v_K \left[1 - \left(\frac{H}{r} \right)^2 \left(1 - \frac{\partial \ln \rho_g}{\partial \ln r} \right) \right]^{1/2}, \quad (28)$$

which reduces to Equation (27) for the unperturbed disk case. Figure 3 and Equation (28) suggest that the magnitude of the gradient $\partial \ln \rho_g / \partial \ln r$ is marginally larger at the outer edge of the gap than it is at the inner edge. If a particle moved at a Keplerian speed, on average it would experience a tail wind when orbiting near the outer edge of the density gap and a head wind when orbiting near the inner gap edge.

5.1. Circumplanetary Disk Thermodynamics

Let us introduce a local reference frame $\{\mathcal{O}'; x, y, z\}$, with origin \mathcal{O}' on the planet, coordinate x pointing away from the star, y pointing toward the direction of orbital motion, and z pointing away from the disk's equatorial plane ($\theta = \pi/2$) in the direction $\theta = 0$.

The normalized density, ρ_g/ρ_0 , is illustrated in Figure 4, on length scales $\lesssim R_H$, on vertical (top) and equatorial (bottom) slices passing through the position of the planet. The density contour levels in the lower panels of the figure indicate that a perturbation in the form of a spiral wave propagates toward the planet, but it does not propagate in the inner disk, within a distance of $0.1 R_H$, or about $75 R_J$ of the planet. This is in agreement with previous 3D calculations. Note that while all of Jupiter's regular satellites orbit inside $30 R_J$ of the planet, irregular satellites have semi-major axes between $\sim 100 R_J \approx 0.13 R_H$ and $\sim 425 R_J \approx 0.56 R_H$ (e.g., Jewitt et al. 2004; Jewitt & Haghighipour 2007). Beyond $\sim 240 R_J \approx 0.32 R_H$, these satellites are all on retrograde orbits.

Line plots of the vertical density distribution are shown in the top panel of Figure 5, at various distances from the planet's location (see figure caption for details). The volume and surface densities within the inner Roche lobe are shown in the middle and bottom panels, respectively. A close-up of these quantities around the planet can be seen in the insets. The surface density between ≈ 0.02 and $\approx 0.15 R_H$ of the planet roughly declines as a -0.3

power of the distance. This slope becomes approximately -1 between ≈ 0.15 and $\approx 0.5 R_H$.

The two-dimensional models of D'Angelo et al. (2003a) showed that circumplanetary disks are typically thick, with an aspect ratio ranging from ~ 0.2 to ~ 0.4 , depending on the thermal state of the disk. This conclusion was later confirmed by several other studies (e.g., Machida et al. 2008; Ayliffe & Bate 2009; Martin & Lubow 2011; Tanigawa et al. 2012). The top-right panel of Figure 4 also predicts a thick disk, in agreement with previous results. A direct measurement from the data in the figure, of the location where there is a sharp density drop, yields an aspect ratio of about 0.36 within $\approx 0.13 R_H$ of the planet.

Although we use a local isothermal equation of state (Equation (2)), which becomes effectively isothermal in the small region around the planet occupied by the circumplanetary disk, we set a gas temperature using simple arguments based on local heating via viscous dissipation and black-body radiation from ambient gas, and vertical radiative cooling. Indicating with $\tilde{r}^2 = x^2 + y^2$, the effective disk temperature, T_e , is given by (Pringle 1981)

$$T_e^4 - T_n^4 = \frac{3}{8\pi} \frac{GM_p \dot{M}_p}{\sigma_{SB} \tilde{r}^3} \left(1 - \sqrt{\frac{R_p}{\tilde{r}}} \right), \quad (29)$$

where T_n refers to the circumstellar disk temperature in Equation (3) and $R_p = 1.6 R_J$. The maximum of the right-hand side of Equation (29) is $\approx 0.00677 GM_p \dot{M}_p / (\sigma_{SB} R_p^3)$ and occurs at $\tilde{r} = (49/36) R_p$. The gas accretion rate on the planet, measured from the calculation (see Section 4.3), is $\dot{M}_p \approx 2 \times 10^{-5} \Omega_p a_p^3 \rho_0$. However, the accretion rate involved in Equation (29) is actually that through the disk, which is only a small fraction of \dot{M}_p (as mentioned in Section 4.3). Although this fraction varies with distance from the planet, based on the analysis of Tanigawa et al. (2012), we simply approximate it to about 1/6. Since there is no physical boundary at R_p , the interface between the disk and the planet, for $\tilde{r}^2 + z^2 \leq R_p^2$ we set T_e equal to 600 K, the effective temperature of a protojupiter right after most of the envelope has been accreted⁶ (Lissauer et al. 2009). We neglect possible heating effects in the circumplanetary due to irradiation by the planet.

Following Lunine & Stevenson (1982), the vertical temperature can be derived by considering energy transfer via radiation in the vertical direction, which leads to the equation

$$\frac{dT_g^4}{dz} = -3\rho_g \kappa_R (T_e^4 - T_n^4) \left(\frac{z}{\tilde{H}} \right), \quad (30)$$

where κ_R is a frequency-integrated opacity, which we approximate as the Rosseland mean opacity, and $\tilde{H} \approx 0.36 \tilde{r}$ is the local circumplanetary disk scale height (see top panels of Figure 4). By solving Equation (30), we

⁶ In the models of Lissauer et al. (2009), the effective temperature of a protojupiter, after most of the gaseous envelope has been acquired, may initially depend on the accretion history of the planet, but it subsequently converges to ~ 600 K within a few 10^5 years (see their Figure 10) and to ~ 500 K by 10 Myr (Marley et al. 2007).

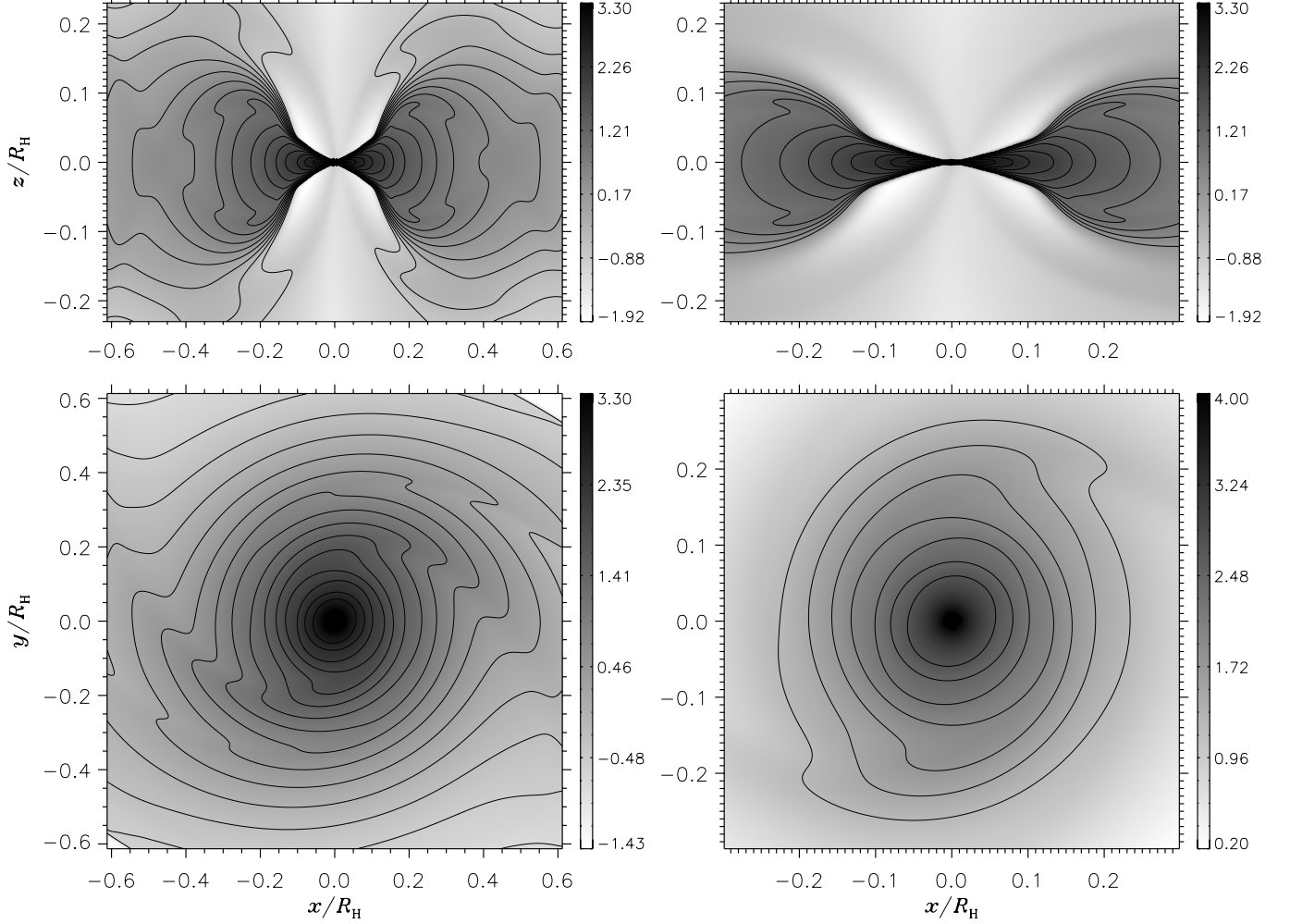


Figure 4. Color scale rendering of $\log(\rho_g/\rho_0)$ on disk slices passing through the planet's location. Vertical slices are illustrated in the top panels whereas slices in the equatorial plane are illustrated in the bottom panels. All distances from the planet are in units of the planet's Hill radius, $R_H \simeq 0.0689 a_p$.

have

$$T_g^4 = T_e^4 + \frac{3}{2} \tau_R(z) (T_e^4 - T_n^4) \left(\frac{\tilde{H} + |z|}{\tilde{H}} \right), \quad (31)$$

with a height-dependent optical depth $\tau_R = \bar{\rho}_g \kappa_R (\tilde{H} - |z|)$, assumed to be non-negative. The quantity $\bar{\rho}_g$ is a vertically averaged volume density between heights $|z|$ and \tilde{H} . Although the equation above is derived for a vertically constant opacity, we assume that κ_R is either constant or a linear function of T_g . Thus, the solution of Equation (31) typically requires a root-finding iteration procedure, for which we use an algorithm based on the Brent's method (Brent 1973).

We recall that, in Equation (31), T_g indicates the temperature in the circumplanetary disk, T_n is the temperature in the circumstellar disk (Equation (3)), and $T_e^4 - T_n^4$ is given by Equation (29). At $|z| = \tilde{H}$, we have that $T_g = T_e$ whereas, for $|z| > \tilde{H}$, we impose an exponential decline over height of T_g until it matches T_n .

The underlying local isothermal approximation used in the hydrodynamics calculations implies that the opacity

of the medium (gas+dust) is low. If we apply a gas-dominated opacity, $\kappa_R = 10^{-4} \text{ cm}^2 \text{ g}^{-1}$, as contemplated in some of the models of Canup & Ward (2002), then T_g becomes about equal to the effective temperature T_e , as can be seen by comparing the red and blue curves in the two panels of Figure 6.

In Equation (31), as anticipated above, we use an opacity that is a piece-wise function of the temperature. Below the vaporization temperature of dust grains (Pollack et al. 1994), we set $\kappa_R = 0.01 \text{ cm}^2 \text{ g}^{-1}$, which may be the case in an evolved disk where grains have undergone significant growth (e.g., D'Alessio et al. 2001). We assume that κ_R linearly transitions to a gas-dominated opacity, $\kappa_R = 10^{-4} \text{ cm}^2 \text{ g}^{-1}$, in the temperature interval from 1600 K to about 2000 K, and it remains constant at larger temperatures. For this opacity law, the equatorial temperature of the circumplanetary disk is illustrated as a black line in Figure 6, for both reference background densities $\rho_0 = 10^{-12}$ (top) and $10^{-11} \text{ g cm}^{-3}$ (bottom). At distances from the planet $\tilde{r} \gtrsim 0.2 R_H$, the radial distribution of temperature merges with the temperature distribution in the circumstellar disk.

Since Equation (31) is not consistent with the equa-

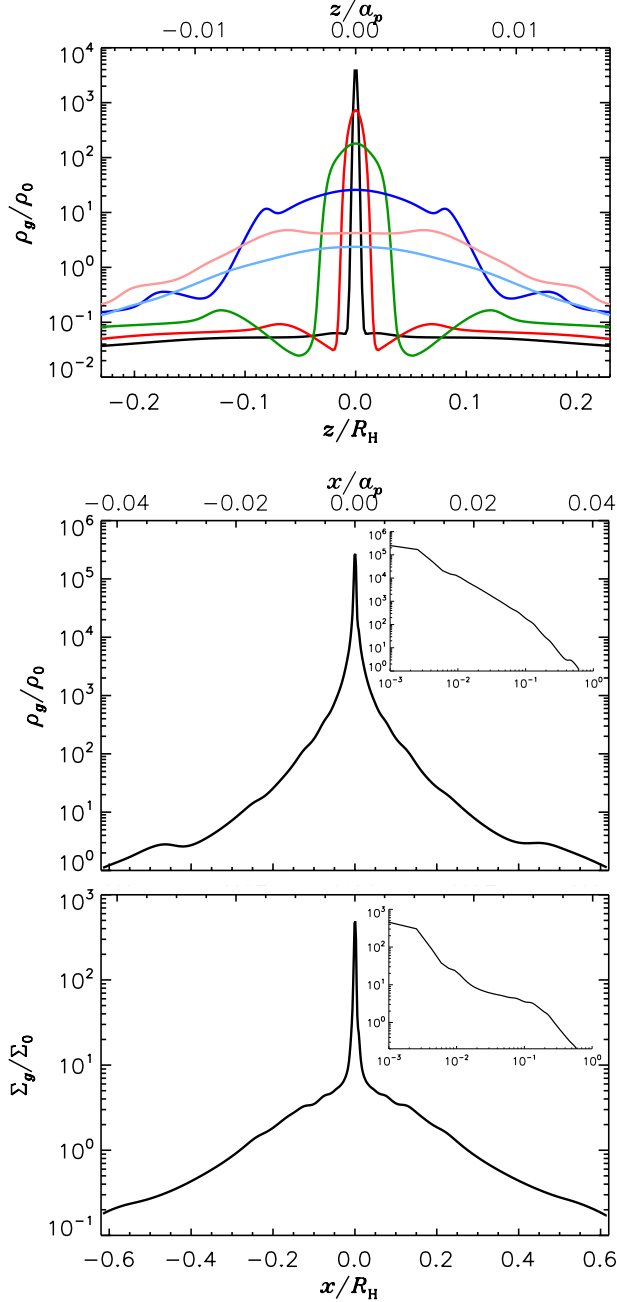


Figure 5. The top panel shows the normalized volume density, ρ_g/ρ_0 , along the vertical direction at various distances from the planet. From profiles with lower to higher peak density, the distance is 0.5, 0.35, 0.2, 0.1, 0.05, and 0.02 R_H . The middle and bottom panels show, respectively, the normalized the (mid-plane) volume and surface density around the planet. The top x -axis of each panel gives the distance in units of the planet’s semi-major axis, a_p , while the bottom axis is in units of R_H .

tion of state applied in the hydrodynamics calculations (Equation (2)), we also consider cases in which the gas temperature is given everywhere by Equation (3). In these calculations, the circumplanetary disk is basically isothermal with a gas temperature $T_n \simeq (\mu_g m_H / k_B)(GM_*/a_p)(H/a_p)^2$. The lower temperature close to the planet may affect the ablation history, and hence the mass evolution, of some planetesimals.

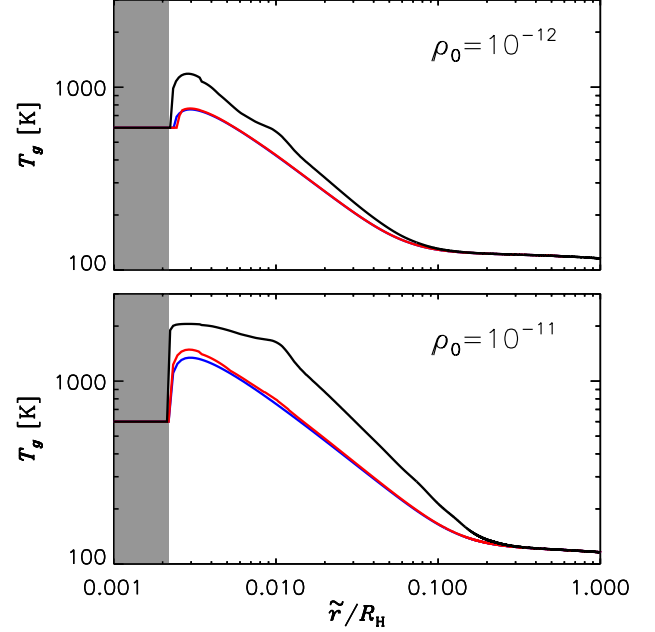


Figure 6. Temperature in the equatorial plane of the circumplanetary disk, from Equation (31), as a function of the distance from the planet, for background volume density $\rho_0 = 10^{-12} \text{ g cm}^{-3}$ (top) and $10^{-11} \text{ g cm}^{-3}$ (bottom). The shaded areas indicate distances $\tilde{r} < R_p$. The black curves use a Rosseland mean opacity $\kappa_R = 10^{-2} \text{ cm}^2 \text{ g}^{-1}$ for $T_g < 1600 \text{ K}$, which decreases linearly toward a gas-dominated opacity ($\kappa_R = 10^{-4} \text{ cm}^2 \text{ g}^{-1}$). The red curves are for a constant, gas-dominated opacity $\kappa_R = 10^{-4} \text{ cm}^2 \text{ g}^{-1}$, while the blue curves represent the effective disk temperature, T_e (Equation (29)).

6. EVOLUTION OF PLANETESIMALS IN THE CIRCUMSTELLAR DISK

We follow the evolution of planetesimals initially equally distributed in four size bins with radii $R_s = 0.1, 1, 10$, and 100 km . The planetesimals are placed on elliptical orbits about the star. The initial orbital eccentricity, e_s , and inclination, i_s , are randomly selected within the range from 0 to 0.05 and from 0 to 0.05 radians ($\approx 2.9^\circ$). The initial argument of periapsis, longitude of the ascending node, and true anomaly are chosen randomly between 0 and 2π . At the beginning, three regions in semi-major axis, a_s , are populated: from $0.77 a_p$ to $0.82 a_p$, from $0.965 a_p$ to $1.035 a_p$, and from $1.2 a_p$ to $1.25 a_p$. These regions are all inside $4 R_H$ of the planet’s orbit, the classical “feeding zone” for accretion of solids (e.g., Greenzweig & Lissauer 1990; Lissauer & Stewart 1993). Planetesimals deployed in the corotation region of the planet, $a_p \mp R_H/2$, have near-circular orbits and are deployed with an azimuth such that $|\phi - \phi_p| > \pi/3$, i.e., in between the triangular Lagrange points L_4 (leading) and L_5 (trailing). These three regions are each populated with 132000 planetesimals (for a total of 0.65 or 0.86 Mars masses of solids, depending on the material). Initial surface densities of solids are between ≈ 0.05 and $\approx 0.12 \text{ g cm}^{-2}$, depending on the region and the material. It is important to stress that, given the equal number densities per size bin, the solid mass is almost entirely carried by the largest bodies. Icy and mixed-composition planetesimals are considered in separate cal-

culations. The results presented here can be rescaled by the initial surface density of solids, provided that interactions among planetesimals can be neglected (see Section 6.1).

In a planet-less disk, the orbital evolution of planetesimals would be dictated only by gas drag (and stellar gravity). Thus, orbital eccentricity and inclination would be damped on a timescale $\tau_{\text{damp}} \sim |\mathbf{v}_s - \mathbf{v}_g|/|\mathbf{a}_D|$. In a nearly Keplerian disk, with negligible radial velocity and with azimuthal velocity given by Equation (27), the approximation $|\mathbf{v}_s - \mathbf{v}_g| \sim (5e_s^2/8 + i_s^2/2 + \xi^4/4)^{1/2} a_s \Omega_K$ can be adopted, where $\xi^2 = (5/2)(H/r)^2$ and Ω_K is the Keplerian orbital frequency of the planetesimal about the star (e.g., Adachi et al. 1976; Ogiwara & Ida 2009). Therefore,

$$\frac{1}{\Omega_K \tau_{\text{drag}}} \sim \frac{3}{8} C_D \left(\frac{a_s}{R_s} \right) \left(\frac{\rho_g}{\rho_s} \right) \sqrt{\frac{5}{8} e_s^2 + \frac{1}{2} i_s^2 + \frac{1}{4} \xi^4}. \quad (32)$$

The timescale for the removal of orbital energy, and hence for the variation of the planetesimal semi-major axis, is much longer, of order τ_{drag}/ξ^2 (see also Equation (B5)). Our initial conditions (e_s and $i_s \leq 0.05$) would lead to damping timescales, at ~ 5 AU and for $\rho_0 = 10^{-11} \text{ g cm}^{-3}$, $\tau_{\text{drag}} \gtrsim 20$ orbits for ~ 0.1 km-size bodies ($C_D \approx 6$) and $\gtrsim 2 \times 10^5$ orbits for ~ 100 km-size bodies ($C_D \approx 0.4$). It is worth noticing, however, that Equation (32) assumes that ρ_g is constant along the trajectory of the planetesimal. The timescales for drag-induced orbital decay would be over two orders of magnitude as long. The planetesimal evolution presented here lasts for ≈ 580 planet's orbits, or ≈ 7000 years. Although the initial orbits of planetesimals are arbitrary, by the end of the calculations the spatial distributions of the solids are in a state of quasi-equilibrium, in the sense that they vary slowly over tens of orbital periods of the planet. Over much longer timescales, the lack of a supply of planetesimals from other regions (besides those considered here) likely inhibits a state of true dynamical equilibrium.

The distributions of some instantaneous (osculating) orbital elements are presented in Figures 7 and 8, at the end of the evolution (see the figure captions for further details). The histograms refer to bodies deployed in the regions interior and exterior of the planet's orbit (Figure 7) and in the planet's corotation region (Figure 8). Bodies that move beyond the disk boundaries (see Section 2) are removed from the calculations and excluded from the analysis. Between $\approx 11\%$ and $\approx 14\%$ of the initial mass in solids moves out of the computational domain by the end of the calculations, where the larger percentage is generated by cases with $\rho_0 = 10^{-12} \text{ g cm}^{-3}$ (icy and mixed-composition bodies produce similar fractions). The average rates of mass loss through the boundaries, between 2% and 3% of the initial mass per 100 orbits, are consistent with those measured over the last 100 orbits of the calculations. The probability of ejecting out of boundaries bodies of ~ 10 – 100 km in radius is similar (within factors of order unity), and higher or somewhat higher (depending on ρ_0) than the probability of ejecting $R_s \lesssim 1$ km bodies.

During the evolution, only about 0.3% of the initial mass is ablated. The rates of mass lost to ablation are roughly steady during the course of the calculations.

Higher gas densities produce slightly more ablation than do lower densities. Models that use everywhere the gas temperature given by Equation (3), instead of the locally modified temperature discussed in Section 5.1, yield similar fractions for the ablated mass (see Section 7.1). The small percentage of ablated mass masks the fact that the total mass in solids is basically carried by 100 km bodies, which shed relatively little mass. Smaller bodies, however, are more prone to ablation. In fact, $R_s \approx 10$ km bodies lose $\sim 5\%$ of their total initial mass and $R_s \approx 1$ km planetesimals shed $\sim 20\%$ of their total initial mass. The fraction becomes $\sim 40\%$ for $R_s \approx 0.1$ km bodies. This outcome can be understood from Equation (19), assuming bodies of equal temperature (and hence vapor pressure, P_v), which yields a ratio of the ablated to the total mass proportional to $1/R_s$. Had all size bins contained equal masses, the swarm would have lost to ablation over 10% of its original mass.

Negligible fractions of the initial mass are lost through fracturing and break-up: $\sim 10^{-6}$ for $\rho_0 = 10^{-12} \text{ g cm}^{-3}$ and $\sim 10^{-5}$ for $\rho_0 = 10^{-11} \text{ g cm}^{-3}$. Bodies can break up only if their radius is smaller than R_{dy} (Equation (25)) and the body's compressive strength is exceeded by the dynamical pressure, P_{dy} , which is proportional to the gas density (Equation (24)). Break-up of planetesimals occurs within $0.2 R_H$ of the planet, when they impact with the dense regions of the circumplanetary disk.

Comparisons of the histograms show only marginal differences between the orbital elements of icy and mixed-composition bodies, for the same value of the gas density ρ_0 . As expected from the discussion above, calculations with $\rho_0 = 10^{-12}$ and $10^{-11} \text{ g cm}^{-3}$ provide similar distributions of semi-major axes, and distributions of eccentricities and inclinations differing mainly toward large values ($e_s \gtrsim 0.5$ and $i_s \gtrsim 5^\circ$). Regardless of the planetesimal composition and background gas density, by the end of the calculations, about 5% of the remaining mass of solids initially placed interior of the planet's orbit is scattered outside the orbit. Toward the end of the calculations, the average scattering rate is about 1% of the remaining mass per 100 orbital periods. Around 11% of the available mass of solids initially present exterior of the planet's orbit is scattered inside, with an average scattering rate (toward the end) of about 6% of the remaining mass per 100 orbits. This would amount to an average of $\sim 10^{24}$ g of solids scattered toward the inner disk during a planet's orbital period, if the initial surface density of planetesimals between $1.2 a_p$ and $1.25 a_p$ was 1 g cm^{-2} . Although scattering involves planetesimals of all sizes, larger size objects ($R_s \gtrsim 1$ km) are typically scattered more efficiently, in either radial direction, than are smaller size objects. Moreover, $R_s \sim 0.1$ km bodies are more easily scattered outward, from inner disk regions, at the lower (rather than at the higher) value of the reference density, ρ_0 . While not visible in the histograms of Figure 7, because of the large bin size, distributions with finer sampling in semi-major axis show several dips, in proximity to the position of the 3:2, 5:3, and 2:1 mean-motion resonances with the planet, and to the corresponding resonant locations exterior of the planet's orbit.

Most of the mass deployed in the corotation region ($a_p \mp R_H/2$) remains within $a_p \mp R_H$ throughout the cal-

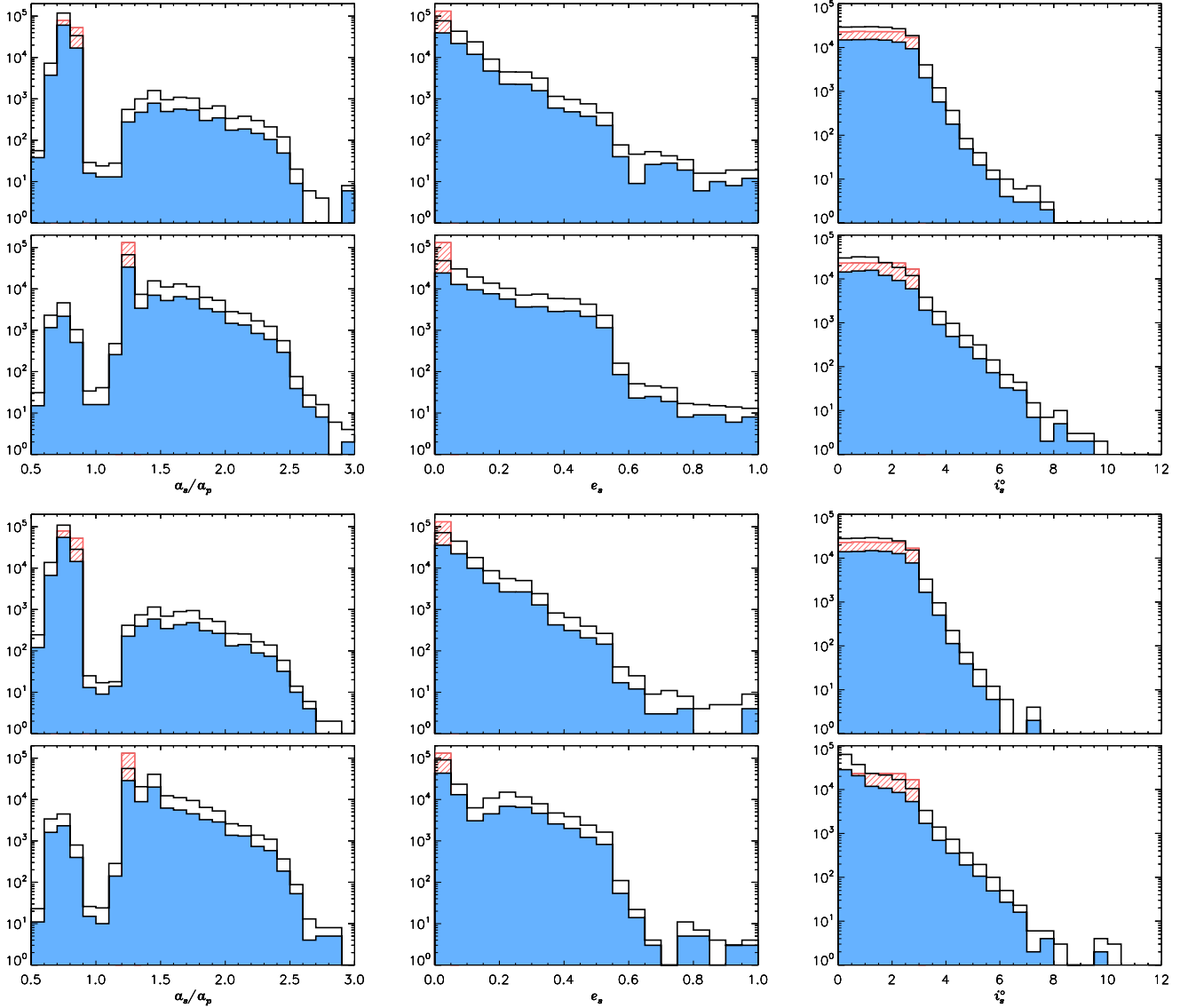


Figure 7. Distributions of semi-major axis (left), eccentricity (center), and inclination (right) for $\rho_0 = 10^{-12}$ (upper pair of rows) and $10^{-11} \text{ g cm}^{-3}$ (lower pair of rows). Odd (even) rows illustrate the distributions of planetesimals deployed in the region inside (outside) of the planet's orbit. The cross-hatched histograms show the initial distributions of the mixed-composition bodies. The color-shaded and line histograms represent the distributions, respectively, of the mixed-composition population and of both the icy and mixed-composition populations, about 580 orbits after deployment.

culations (see Figure 8). Only a small fraction, $\sim 0.5\%$, of the initial mass is scattered toward the inner disk and a fraction of a few percent is scattered outward. Taking into account all possible fates for the solids, the mass depletion rate of the radial region $a_p \mp R_H$ is around 2% of the initial mass per hundred orbits of the planet. Note that gas drag in the region along the planet's orbit is reduced (except very close to the planet) due to the density gap (see Figure 2). Within factors of order unity, the ejection probability toward the inner disk and that toward the outer disk are constant in the size range $0.1 \text{ km} \lesssim R_s \lesssim 100 \text{ km}$. Along the planet's orbit, the largest number densities in the frame corotating with the planet occur around the L_4 and L_5 Lagrange points. Although the longitude relative to the planet of these points can be affected by gas drag, they effectively lie 60° ahead (L_4) and behind (L_5) the planet (for $R_s \gtrsim 0.1 \text{ km}$) owing

to the presence of the density gap (Peale 1993). In the radial region of tadpole orbits, $a_p \mp 0.74 R_H$ (e.g., Murray & Dermott 2000), the number densities within a 15° longitude of either point are roughly constant for planetesimals of all sizes. The smallest number density (in the corotating frame) is around the collinear L_3 point.

The gap in the planetesimal disk, due to the torques exerted by the planet on the solids, is illustrated in Figure 9 as a function of the semi-major axis, for various planetesimal radii (see figure caption for further details). The distributions comprise icy and mixed-composition bodies, initially deployed interior and exterior of the planet's orbit. The positions of the gap edges move further away from the planet's orbit as R_s reduces because of gas drag effects (see below). Differences with respect to the gas density appear marginal for radii $R_s \gtrsim 1 \text{ km}$, but they become more pronounced at radii $R_s \lesssim 0.1 \text{ km}$ (parti-

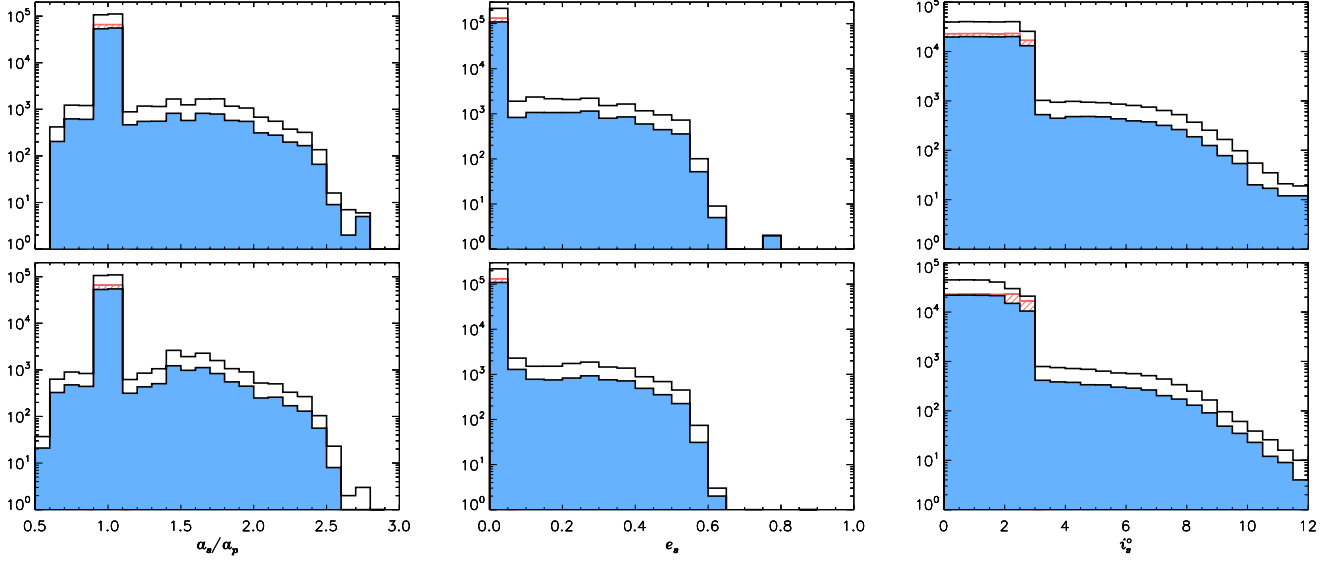


Figure 8. As in Figure 7, but for bodies initially placed in the planet corotation region. Top (bottom) panels refer to $\rho_0 = 10^{-12}$ (10^{-11}) g cm^{-3} .

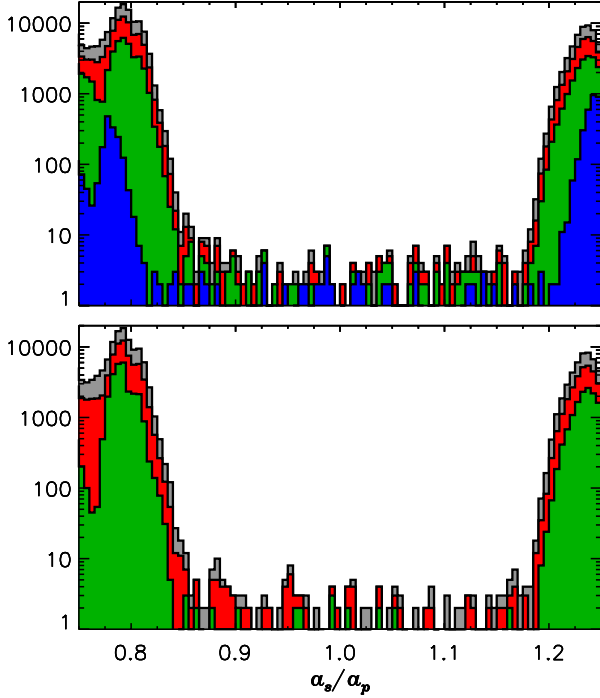


Figure 9. Semi-major axis distributions of planetesimals in proximity of the planet's orbit. The histograms include bodies initially placed inside and outside of the orbit and of both compositions. The reference gas density is $\rho_0 = 10^{-12}$ (top) and 10^{-11} g cm^{-3} (bottom). Histograms of different colors progressively include larger and larger bodies: $R_s \leq 0.1$ (lowest-count histogram), 1, 10, and 100 km (highest-count histogram). In the bottom panel, $R_s \leq 0.1$ km bodies do not appear because they are located farther from the planet's orbit.

cles of these sizes do not appear in the bottom panel of Figure 9). For $\rho_0 = 10^{-11}$ g cm^{-3} , the outer gap edge of $R_s \sim 0.1$ km bodies recedes at $r \approx 1.25 a_p$, where the (azimuthally) averaged rotation velocity of the gas exceeds the azimuthal velocity of particles because the

radial pressure gradient of the gas is locally positive (although only marginally, this effect is already present at $r \sim 1.6 a_p$). The inner gap edge of 0.1 km bodies is found at $r \approx 0.67 a_p$. To address the behavior of small fragments, in Section 8 we discuss some experiments conducted with cm-to-m size particles.

In fact, the super-Keplerian rotation at the outer edge of the density gap, mentioned in Section 5 (see Figure 3), can lead to planetesimal segregation, by halting or pushing outward bodies that reach those radial locations (see, e.g., [Ayliffe et al. 2012](#), and references therein). Neglecting collisions and gravitational encounters among bodies, which would redistribute bodies and likely work against segregation, the efficiency of this process depends on the competing effects of the gravitational torque (perpendicular to the orbital plane) exerted by the planet and the vertical component of the gas drag torque $\mathbf{r}_s \times \mathbf{F}_D$. Considering planetesimals on near-Keplerian orbits, $\mathbf{r}_s \times (\mathbf{v}_g - \mathbf{v}_s)$ has vertical component $\sim a_s(v_\phi^A - v_K)$, where v_ϕ^A is given by Equation (28) (see also Figure 3), which is positive/negative at the outer/inner gap edge. For large enough objects ($C_D \sim 1$), the gas drag torque is then $\propto R_s^2 \rho_g a_s v_K^2 \propto R_s^2 \rho_g$ whereas the gravitational torque due to the planet is proportional to the body mass and hence to R_s^3 , yielding a segregation efficiency $\propto \rho_g / R_s$. Therefore, for a given value of the local density (and distance from the planet's orbit), one can expect segregation of smaller planetesimals to be more efficient than that of larger bodies. As expected, we do not observe strict segregation of planetesimals. However, it does appear that $R_s \sim 0.1$ km bodies, initially placed in the region exterior of the planet's orbit, are less likely to move toward the inner disk than are $R_s \sim 1$ km bodies, by a factor of ~ 10 (see Figure 9, top panel). Additionally, $R_s \sim 0.1$ km bodies are less prone to cross from the outer to the inner disk at the higher value of ρ_0 than they are at the lower density, again by a factor of order 10.

Figure 10 shows two-dimensional histograms of eccentricity, inclination, size, and temperature of planetesi-

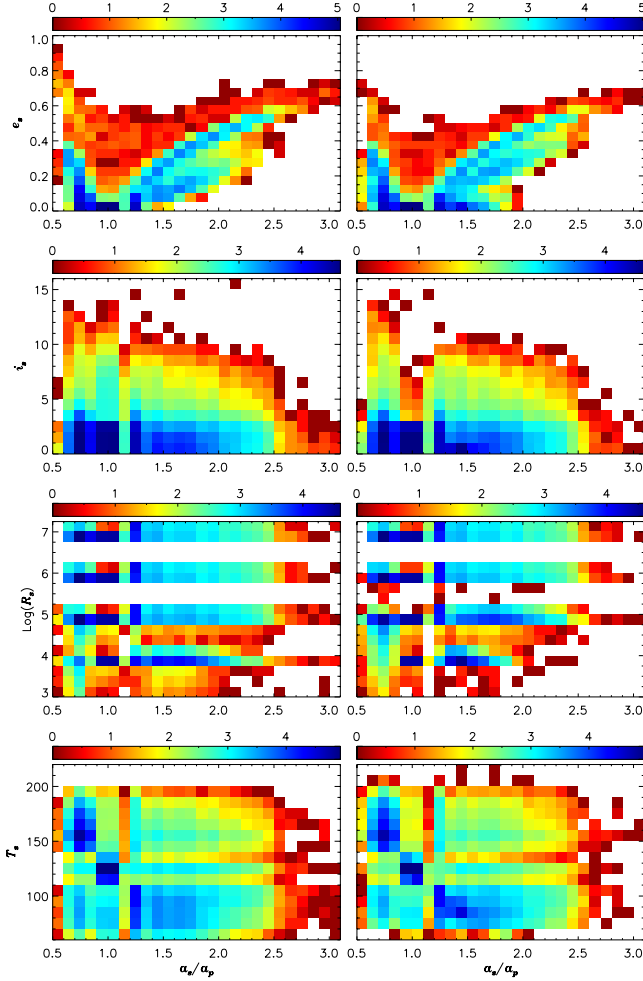


Figure 10. Distribution of icy and mixed-composition particles versus semi-major axis and versus orbital eccentricity, orbital inclination, radius, and temperature, as indicated on the vertical axes. Bodies initially placed inside and outside of the planet’s orbit and in the corotation region are all included. Left and right panels refer, respectively, to the lower and higher gas densities ($\rho_0 = 10^{-12}$ and $10^{-11} \text{ g cm}^{-3}$). The color scale indicates the logarithm of the number of particles. Inclinations are in degrees, radii are in cm and temperatures are in K.

imals versus semi-major axis. The distributions include both icy and mixed-composition bodies, for $\rho_0 = 10^{-12}$ (left) and $10^{-11} \text{ g cm}^{-3}$ (right), initially deployed in all three disk regions mentioned above. As indicated by Figure 7, orbital eccentricities can exceed 0.8 at both gas reference densities, but these values typically occur for $a_s \gtrsim 3 a_p$. Most of planetesimals produced via ablation of initially larger bodies have temperatures $T_s \gtrsim 150 \text{ K}$, which indicates that ablation is ongoing. In some instances, temperatures have settled at lower values, indicating that these planetesimals orbit in colder disk regions. At $T_s \gtrsim 200 \text{ K}$, bodies are consumed relatively rapidly. In fact, below the critical temperature ($T_s < T_{\text{cr}}$), the timescale for ablation of a planetesimal is

$$M_s \left| \frac{dM_s}{dt} \right|^{-1} = \frac{1}{3} \frac{R_s \rho_s}{P_v} \sqrt{\frac{2\pi k_B T_s}{\mu_s m_H}}. \quad (33)$$

In the equation above, for mixed-composition planetes-

imals, P_v is the vapor pressure of ice and μ_s is the mean molecular weight of ice modified by the ice mass fraction. At $T_s = 150 \text{ K}$, the vapor pressure of ice is $\approx 5 \times 10^{-5} \text{ dyne/cm}^2$ and the timescale for ablation of a $R_s = 100 \text{ km}$ body would be in excess of 10^8 years (assuming that T_s remains constant and neglecting recondensation). But this timescale rapidly declines as T_s (and hence P_v) rises, becoming $4\text{--}5 \times 10^3$ years at 200 K ($P_v \approx 1.6 \text{ dyne/cm}^2$) and $\sim 10^3$ years at 210 K ($P_v \approx 7 \text{ dyne/cm}^2$). The distribution of T_s versus a_s in Figure 10 would place the ice line at around 2.8 AU , where the gas temperature $T_g = T_n$ is about 220 K (see Equation (3), although T_s needs not be in equilibrium with T_n). However, global models of evolving disks (e.g., D’Alessio et al. 2005, see also D’Angelo & Marzari 2012) predict somewhat lower gas temperatures in those disk regions at times $\gtrsim 1 \text{ Myr}$. Therefore, the ice line can move inside 2 AU as long as the gas remains optically thick to stellar radiation.

6.1. An Estimate of Collision Rates

The rates of collisions among planetesimals can be derived from simple arguments. The average relative velocity between two bodies in a swarm is such that (e.g., Stewart & Kaula 1980)

$$\langle v_{\text{rel}}^2 \rangle = a_s^2 \Omega_K^2 \left(\frac{5}{8} \langle e_s^2 \rangle + \frac{1}{2} \langle \sin^2 i_s \rangle \right). \quad (34)$$

Based on the two-body approximation, the cross section for collisions of a target planetesimal of radius R_s with those of radius R_j is

$$S_j = \pi (R_s + R_j)^2 \left(1 + \frac{v_{\text{esc}}^2}{\langle v_{\text{rel}}^2 \rangle} \right), \quad (35)$$

where $v_{\text{esc}}^2 = 2GM_s/R_s$. The rate of collisions on the target body is then

$$\frac{dN}{dt} = \sum_j \mathcal{N}_j S_j \langle v_{\text{rel}}^2 \rangle^{1/2}, \quad (36)$$

where \mathcal{N}_j is the number density of solids, which involves the planetesimals’ surface density, Σ_s , and the swarm thickness, $\langle a_s \sin i_s \rangle$. The averages $\langle v_{\text{rel}}^2 \rangle$ and $\langle a_s \sin i_s \rangle$, as a function of a_s , are directly evaluated from the calculations. In a swarm with equal number densities of $0.1\text{--}100 \text{ km}$ bodies, the largest planetesimals have the highest collision rates. In the circumstellar disk, at some distance from the planet’s orbit and for $\Sigma_s \sim 1 \text{ g cm}^{-2}$, during the course of the calculations the number of collisions on any planetesimal would be negligible. The same arguments applied to planetocentric orbits in the circumplanetary disk (see Section 7) would yield a collision rate of $dN/dt \sim 10^{-4} \sqrt{GM_p/a_s^3} (\Sigma_s/1 \text{ g cm}^{-2})$ for $a_s \lesssim 0.15 R_H$.

7. EVOLUTION OF PLANETESIMALS IN THE CIRCUMPLANETARY DISK

Consider the reference frame $\{\mathcal{O}'; x, y, z\}$, introduced in Section 5.1, whose origin is fixed to the planet. Based on relative positions and velocities, we derive the osculating orbital elements in this frame of the planetesimals bound to the planet. Relative trajectories that are not

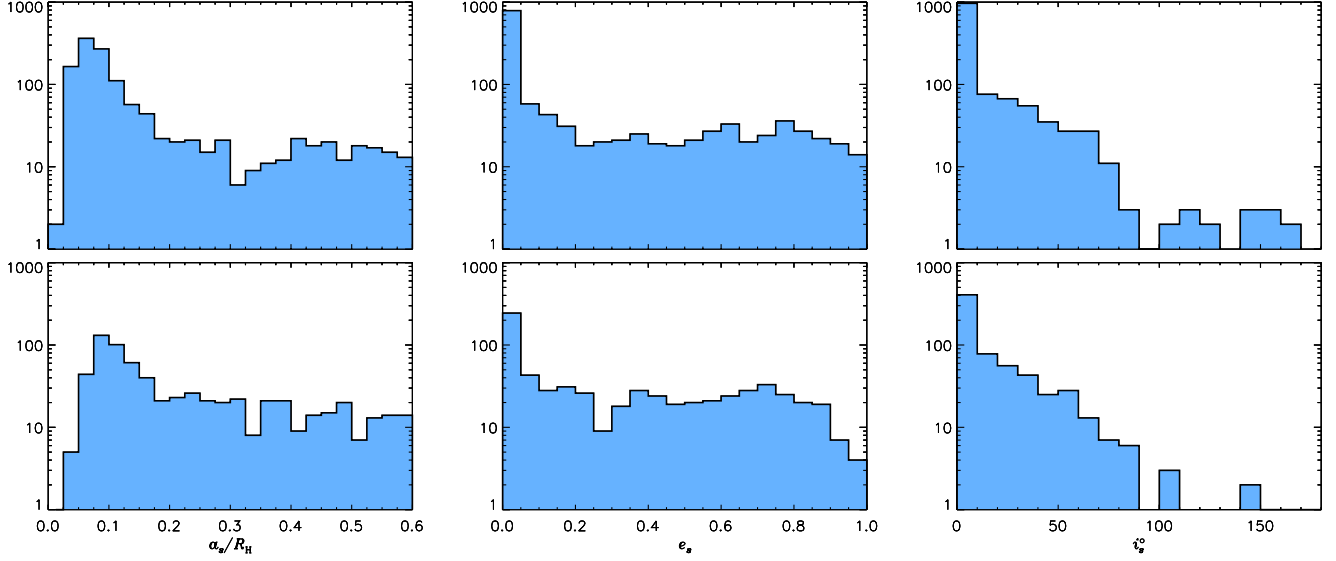


Figure 11. Planetocentric orbital elements, semi-major axis (left), eccentricity (center), and inclination (right), of icy and mixed-composition planetesimals bound to the planet. Top (bottom) panels refer to the density $\rho_0 = 10^{-12}$ (10^{-11}) g cm^{-3} .

representable by osculating ellipses are disregarded, although they may belong to bodies that will accrete on the planet. Notice that we maintain the same notations as in previous sections, even though the orbits are relative to the planet. Since planetesimals are initially placed on orbits about the star well outside the Roche lobe region, these are all objects captured by the planet’s gravity. Capture is aided by dissipation of kinetic energy through gas drag. Figure 11 shows semi-major axes (left), eccentricities (center), and inclinations (right) of these orbits, including both icy and mixed-composition bodies. The top/bottom panels refer to the lower/higher background density, ρ_0 . The histograms include only those objects whose (planetocentric) orbit has a semi-major axis $\leq 0.6 R_H$. Inclination distributions indicate the presence of retrograde orbits ($i_s > 90^\circ$, see also Figure 12). These objects are among those initially moving in the corotation region and in the region exterior of the planet’s orbit, although the absence of retrograde objects originating from the inner disk region may be a result of small-number statistics. As explained below, since the orbital elements are based on osculating ellipses, not all planetesimals represented in Figure 11 are permanently captured (or accreted) by the planet.

The histograms in the top row of Figure 11 include about 1.8 times as many bodies as the histograms in the bottom row. Yet, the distributions for the reference density $\rho_0 = 10^{-11} \text{ g cm}^{-3}$ contain about 25% as much mass (see distributions of R_s in Figure 12). Most captured bodies have radii $\lesssim 10 \text{ km}$, but most of the mass is carried by $R_s \sim 100 \text{ km}$ planetesimals.

Average mass fractions on the order of several times 10^{-4} are captured from the planetesimals initially placed in the inner disk and somewhat larger fractions, $\sim 10^{-3}$, are captured from bodies initially deployed in the region beyond the planet’s orbit. Much smaller mass fractions are instead captured from the corotation region. The fractions are computed as the ratio of the mass of planetesimals moving inside $\tilde{r} \leq 0.6 R_H$ to the total available

mass in solids. Masses are averaged over the last ≈ 50 orbits of the planet. The mass in solids accreted by the planet is not taken into account. This fractional mass may be considered as an “equilibrium” mass between the supply of solids from the circumstellar disk and the mass loss due to ejection, ablation, break-up, and accretion of planetesimals in the circumplanetary disk. If results were rescaled so that the surface density of solids between $0.77 a_p$ and $0.82 a_p$ and between $1.2 a_p$ and $1.25 a_p$ was 1 g cm^{-2} at the end of the calculations, the average mass within $0.6 R_H$ of the planet would be $\sim 10^{-3} M_E$.

Planetesimals that orbit within $\sim 20^\circ$ of the equatorial plane are subject to an increasing drag force, as they approach the planet, due to the augmenting gas density (see Figure 5). Equatorial gas rotation inside $0.1 R_H$ of the planet deviates only a few percent from Keplerian rotation $\sqrt{GM_p/\tilde{r}}$, but the relative difference increases with distance, becoming $\approx 10\%$ at $\tilde{r} \approx 0.2 R_H$ and $\approx 40\%$ at $\tilde{r} \approx 0.5 R_H$. The radial velocity of the gas at the equator is much smaller in magnitude than the azimuthal velocity. For near-circular orbits, gas density can be approximated to a constant and Equation (32) may be applied, although the term in the square brackets of Equation (27) should depend on \tilde{r} in these cases. According to Equation (32), the decay time of orbital semi-major axes due to aerodynamics drag at $\tilde{r} \sim 0.5 R_H$ is on the order of a few times $(R_s/a_s)(\rho_s/\rho_g)$, in units of the local orbital period around the planet. We recall that the length a_s here represents the semi-major axis of the planetocentric orbit. The impact of gas drag on higher inclination orbits ($40^\circ \lesssim i_s \lesssim 140^\circ$) is probably somewhat smaller, since high densities are mostly encountered when these orbits are close the disk’s equatorial plane (see top panels of Figure 4).

Figure 12 shows two-dimensional distributions analogous to those in Figure 10, but for planetesimals bound to the planet. Note that counts of 1, shown in Figure 12, are not visible in histograms of Figure 11, as they lie on the horizontal axis. The figure indicates that plan-

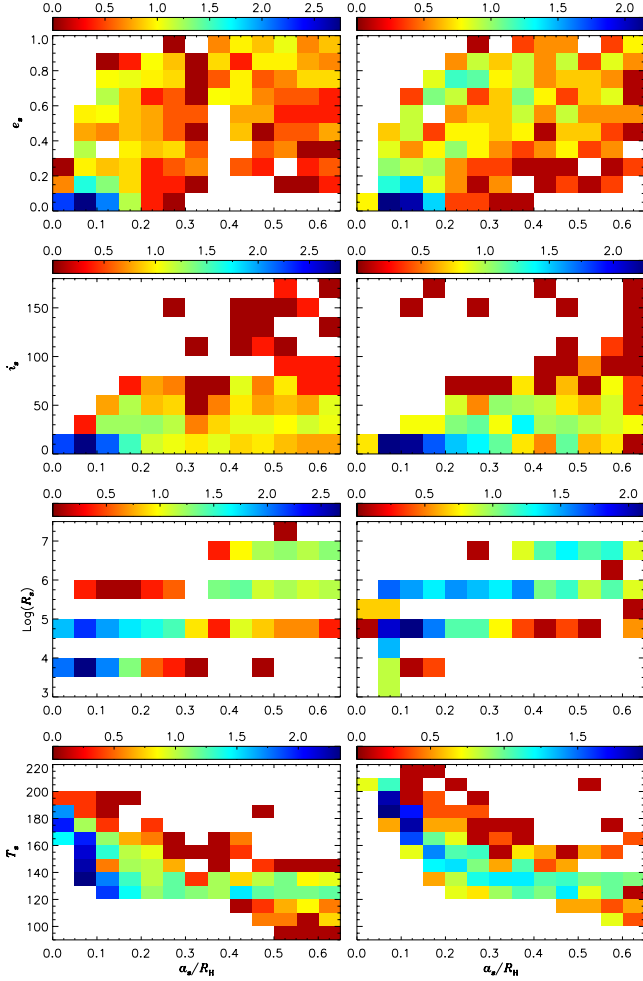


Figure 12. Distribution of icy and mixed-composition planetesimals bound to the planet versus semi-major axis and versus orbital eccentricity, orbital inclination, radius, and temperature, as indicated on the vertical axes. Osculating orbital elements are computed from positions and velocities relative to the planet. Left and right panels refer, respectively, to $\rho_0 = 10^{-12}$ and $10^{-11} \text{ g cm}^{-3}$. The color scale indicates the logarithm of the number of particles. Units are as in Figure 10.

etesimal temperatures are typically $T_s \lesssim 200\text{--}220 \text{ K}$ (see also Figure 13). As argued above, the ablation timescale rapidly decreases at higher temperatures. A finer sampling of the semi-major axis histograms reveals that number densities start to decline inward of $\tilde{r} \approx 0.05 R_H$ and $\approx 0.08 R_H$ for $\rho_0 = 10^{-12}$ and $10^{-11} \text{ g cm}^{-3}$, respectively. Figure 13 shows that particle temperatures (blue circles) become consistently lower than gas temperature (solid line) when substantial ablation begins, as expected from Equation (15) for slowly varying frictional heating and radiative gain/loss energy terms. The gray circles belong to isothermal circumplanetary disk calculations discussed in Section 7.1. The large ablation rates can enrich these circumplanetary disk regions with ice and rock, locally increasing the solid-to-gas mass ratio.

It is safe to assume that, over the course of the calculations, solid material is practically only ablated either inward of 2.8 AU or in close proximity of the planet. By separating these two contributions, we estimate that $\sim 10^{-7} M_E \text{ yr}^{-1}$ worth of ice and silicates would be released in the gas close to the planet, if the initial surface

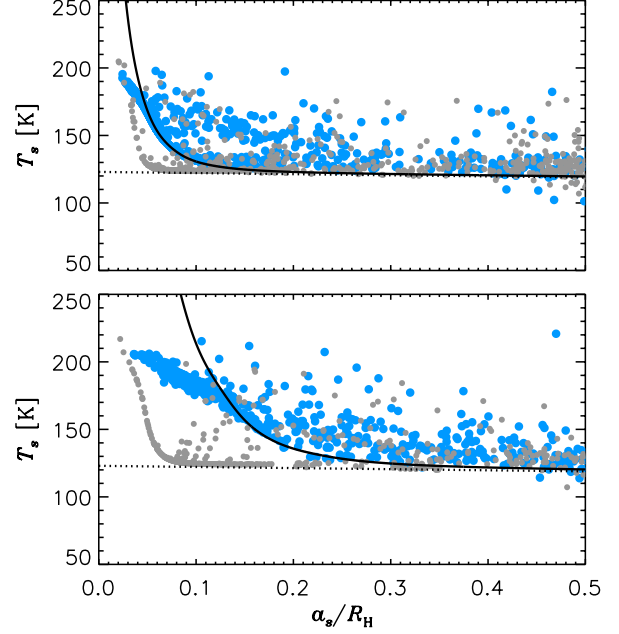


Figure 13. Temperature versus semi-major axis of some planetesimals bound to the planet (blue circles) for the reference gas density $\rho_0 = 10^{-12}$ (top) and $10^{-11} \text{ g cm}^{-3}$ (bottom). The light gray circles indicate the temperature of planetesimals in the isothermal circumplanetary disk calculations (see Section 7.1). The solid lines represent the gas temperature T_g in Equation (31), also plotted in Figure 6. The dotted line is the gas temperature T_n in Equation (3) that, in the “isothermal” calculations, is applied everywhere in the disk.

density of planetesimals between $0.77 a_p$ and $0.82 a_p$ and between $1.2 a_p$ and $1.25 a_p$ was 1 g cm^{-2} . At this production rate, the average metallicity of the circumplanetary disk would become $\sim 0.01 (10^{-12} \text{ g cm}^{-3} / \rho_0)$ in ~ 100 planet’s periods. There are only marginal differences in the amounts of material ablated from icy and mixed-composition bodies ($\sim 10\%$, roughly consistent with the predictions from Equation (33) if equal temperature bodies are assumed) and similar differences are obtained for the two values of ρ_0 .

In the calculations, scattering of planetesimals out of the Roche lobe occurs through interaction with the planet, following one or more close encounters. In Figures 11 and 12, both low and high eccentricity orbits may eventually lead to scattering events. Of the objects plotted in the upper panels of Figure 11, by following the subsequent evolution of a sample, we estimate that the ratio of accreted to scattered (out of the planet’s Roche lobe) objects is about $1/7$. The $R_s \sim 100 \text{ km}$ planetesimals, which are the least affected by gas drag, are those most easily ejected. Bodies are scattered both inward and outward of the planet’s orbit. In this sample, whose initial positions and velocities are the same as those used to draw the distributions in Figure 11, the majority of scattered bodies with a starting semi-major axis $\gtrsim 0.3 R_H$ have eccentricities $\gtrsim 0.6$. To give an idea of the spatial distribution of scattered objects, Figure 14 shows the positions along the trajectories of 18 such bodies, of radius ~ 10 and $\sim 100 \text{ km}$ (see figure caption for details), extracted from said sample. In particular, the planetesimals in the figure are originally placed exterior

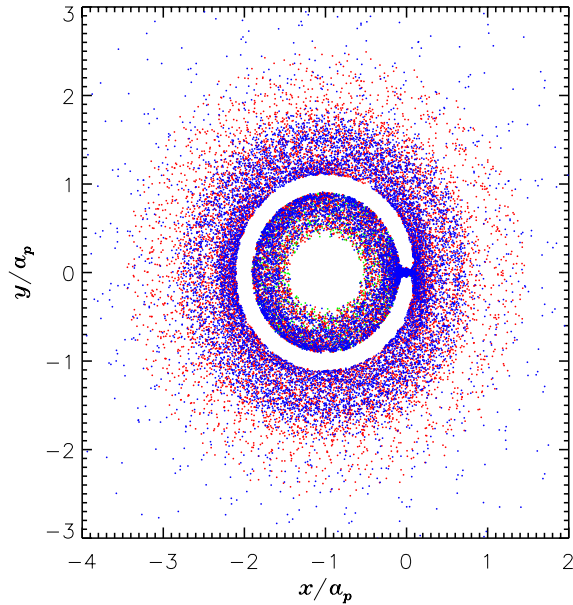


Figure 14. Positions along 18 trajectories, in a reference frame fixed to the planet (Section 5.1), of icy planetesimals scattered out of the planet’s Roche lobe. The star is located at $(x, y) = (-a_p, 0)$. The reference density in the disk is $\rho_0 = 10^{-12} \text{ g cm}^{-3}$. The trajectories are integrated for about 57 orbital periods of the planet. The color scale of the dots indicates the planetesimals radius (which increases from lighter to darker dots). Except for one planetesimal ($R_s \sim 1 \text{ km}$, scattered inward), about equal numbers of bodies have radii ~ 10 and $\sim 100 \text{ km}$.

of the planet’s orbit, before being diverted toward the circumplanetary disk (but all trajectories illustrated in the figure start from within $0.6 R_H$ of the planet).

Table 6 lists the accretion rates of planetesimals on the planet, estimated over the last 50–70 planet’s revolutions. The accretion rates are rescaled so that the average surface density of solids in the regions $0.77 \leq r/a_p \leq 0.82$, $0.965 \leq r/a_p \leq 1.035$, and $1.2 \leq r/a_p \leq 1.25$ is 1 g cm^{-2} . Contributions from each of the three regions are listed separately. There are relatively small differences ($\lesssim 10\%$) between the values obtained from calculations using different reference gas densities, ρ_0 , and different material compositions. The accretion of solids arises almost entirely from the regions interior and exterior of the planet’s orbit, the former region contributing around 5% of the total. The corotation region provides only a minimal fraction of the solids’ accretion. Adding up the regional contributions and averaging out the results, we have

$$\langle \dot{M}_p \rangle_s = 2.8 \times 10^{-5} \left(\frac{\Sigma_s}{1 \text{ g cm}^{-2}} \right) M_E \text{ yr}^{-1}, \quad (37)$$

where Σ_s is the surface density of solids in the three radial regions mentioned above. This result applies for initial planetesimal populations with equal numbers of bodies per size bin. Additionally, as stressed in the previous section, planetesimal-planetesimal interactions are neglected and, therefore, Equation (37) is valid as long as the effects of collisions and encounters among solids can be neglected, i.e., for low enough values of Σ_s . But in absence of a mechanism (like collisions and gravita-

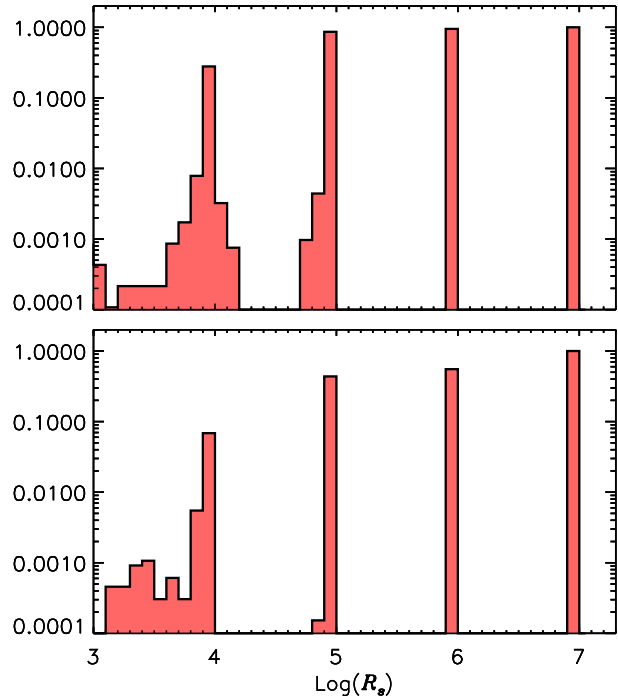


Figure 15. Distributions of the radii of planetesimals accreted by the planet during the course of the calculations. The histograms include bodies of both compositions, initially placed in all three disk regions. The reference gas density is $\rho_0 = 10^{-12}$ (top) and $10^{-11} \text{ g cm}^{-3}$ (bottom). The radii are in cm. Histograms are normalized so that the maximum is 1.

tional stirring) to replenish the exterior disk region with solids (resupply via gas drag would not be effective at the gas density levels considered here due to long orbital decay times, see Section 6), a total mass in solids of order $0.2 \Sigma_s / (1 \text{ g cm}^{-2}) M_E$ can be delivered to the planet. A somewhat smaller mass would be accessible from the interior disk, but over a much longer timescale. This amount of solids may represent only a relatively small addition to the heavy element content of the planet.

The histograms in Figure 15 show the radii in cm of accreted planetesimals for $\rho_0 = 10^{-12}$ (top) and $10^{-11} \text{ g cm}^{-3}$ (bottom). Histograms are rescaled so that the maximum count is 1. For the lower reference density case, there is an almost equal probability, within $\lesssim 15\%$, of accreting bodies in the size range $1 \text{ km} \lesssim R_s \lesssim 100 \text{ km}$. The difference increases for the higher reference density case, in which the probability of accreting $R_s \approx 1 \text{ km}$ bodies is about half that of accreting $R_s \approx 100 \text{ km}$ bodies. (As discussed below, one reason for the different accretion probability lies in the fact that smaller bodies are more likely to break up.) Consequently, our choice of starting the planetesimal populations with equal numbers of objects in different size bins determines the result that the accretion rate in solids is basically supplied by the largest planetesimals. In fact, the accretion rate in Equation (37) is basically that of the largest planetesimals and Σ_s is the surface density of the largest bodies. Therefore, Figure 15 implies that, within factors of order unity, Equation (37) provides the accretion rates of a mono-size population of planetesimals (whose radius belongs to the approximate range 1–100 km) with Σ_s being

Table 6
Accretion Rates of Planetesimals on the Planet^a

Zone	Icy Bodies		Mixed Bodies	
	$\rho_0 = 10^{-12}$	10^{-11}	$\rho_0 = 10^{-12}$	10^{-11}
Interior	1.2×10^{-6}	1.0×10^{-6}	1.2×10^{-6}	1.5×10^{-6}
Corotat.	8.7×10^{-7}	8.2×10^{-7}	8.8×10^{-7}	7.1×10^{-7}
Exterior	2.7×10^{-5}	2.6×10^{-5}	2.4×10^{-5}	2.7×10^{-5}

^a In units of $M_{\text{E}}\text{yr}^{-1}$ and scaled to $\Sigma_s = 1 \text{ g cm}^{-2}$.

the surface density of that population. Figure 15 includes all planetesimals accreted during the course of the calculations, hence it contains some bias due to the choice of the initial distributions of planetesimals. For example, the probability of delivering to the circumplanetary disk, and thus of accreting, $R_s \sim 0.1 \text{ km}$ bodies declines over time because of the widening gap in solids of this size (see Figure 9).

The initial semi-major axis, eccentricity, and inclinations of accreted planetesimals are plotted in Figure 16 (see figure caption for details). The results indicate that planetesimals deployed in proximity of the edge closer to the planet's orbit are more likely to be accreted than are more distant bodies (see left columns). For bodies released in the corotation region (not shown in the figure), the trend is opposite, as expected, due to the stability of tadpole orbits. The probability of accreting planetesimals deployed exterior of the planet's orbit is fairly independent of the initial eccentricity, whereas (in the range 0–0.05) larger initial eccentricities favor accretion of bodies deployed interior of planet's orbit (see center columns). Initially co-planar orbits lead to accretion more easily than do inclined orbits (see right columns). The smaller accretion rates provided by the interior disk (see Table 6) can be explained by observing that the peak number densities around the inner edge of the solids' gap are at $\approx 0.8 a_p$ (see Figure 9), where the probability of accretion is relatively low (see Figure 16, left-even panels).

As mentioned in the previous section, break-up of planetesimals may occur when they encounter the dense gas of the circumplanetary disk, inside $\approx 0.2 R_{\text{H}}$ of the planet (see Figure 5). Assuming that planetesimal fragments can quickly drift toward the planet, the mass of disrupted bodies would contribute to the accretion rate of solids on the planet. However, this addition would amount to $\sim 0.01\%$ or $\sim 0.1\%$ (depending on ρ_0 , see above) of the values reported in Table 6. This small contribution largely depends on the fact that accretion of solids is dominated by $R_s \approx 100 \text{ km}$ planetesimals, which do not tend to break up. However, smaller bodies break up more easily. In fact, for $\rho_0 = 10^{-11} \text{ g cm}^{-3}$, the mass of shattered planetesimals with radii $1 \text{ km} \lesssim R_s \lesssim 10 \text{ km}$ is comparable to (and sometimes larger than) the accreted mass contributed by bodies of these sizes. Thus, if fragments ought to be considered as accreted material, the accretion rate in this size range (e.g., given by Equation (37) applied to a mono-size population) may be higher by a factor of up to a few. For the reference density $\rho_0 = 10^{-12} \text{ g cm}^{-3}$, break-up of planetesimals is less relevant, and it would contribute $\sim 10\%$ to the accretion of $R_s \sim 10 \text{ km}$ bodies and even less to the accretion of

smaller planetesimals.

7.1. Isothermal Circumplanetary Disk Calculations

As anticipated in previous sections, we also consider models that apply the temperature T_n in Equation (3) also in the circumplanetary disk, which then becomes nearly isothermal with a temperature of $\approx 120 \text{ K}$ (see Figure 6 at $\tilde{r} \approx R_{\text{H}}$ and the dotted line in Figure 13). A smaller number of bodies is released in these calculations. Since the gas density is the same as in the models discussed above, differences may be expected especially in the thermal evolution and ablation of planetesimals moving in close proximity of the planet. Nonetheless, we find that there are not large differences between the two approaches.

As above, average fractions of order 10^{-3} are captured within $0.6 R_{\text{H}}$ of the planet from the available mass of planetesimals. More bodies are captured at the lower reference density, ρ_0 , but a somewhat larger mass is retained at the higher value of ρ_0 . Most of the captured bodies have radii $\lesssim 10 \text{ km}$, but most mass is carried by the 100 km -radius planetesimals.

The gray circles in Figure 13 show the planetesimal temperatures as a function of the planetocentric semi-major axis, while the dotted line represents the local gas temperature (see Equation (3)). In the calculations with reference density $\rho_0 = 10^{-12} \text{ g cm}^{-3}$, T_s is generally comparable with the planetesimals' temperature obtained from the calculations discussed above (top panel, darker circles), which use the gas temperature in Equation (31). For the higher reference density, the discrepancy is larger, but only when $0.03 R_{\text{H}} \lesssim a_s \lesssim 0.2 R_{\text{H}}$ (see bottom panel). Body temperatures become comparable again ($T_s \gtrsim 200 \text{ K}$) when planetesimals get close to the planet ($a_s \lesssim 0.03 R_{\text{H}}$), where ablation is most vigorous. It is possibly for this reason that the amounts of ablated material are similar in the two sets of calculations.

The accretion rates of planetesimals on the planet are comparable to those given by Equation (37). Relative differences between isothermal and non-isothermal calculations of accretion rates versus R_s are also small, $\lesssim 20\%$.

The thermal distribution of the gas does not directly affect the fragmentation of planetesimals, as neither the dynamical pressure, P_{dy} , nor the material compressive strength, $\sigma_s \sqrt{1 \text{ km}/R_s}$, is explicitly dependent on T_g (T_n) or T_s . Indirect effects may nonetheless occur, e.g., because of different ablation histories. Consistently with the results presented above, break-up of planetesimals occurs in the proximity of the planet, and mostly in the size range $1 \text{ km} \lesssim R_s \lesssim 10 \text{ km}$. Overall, solid material made available through break-up would only contribute negligibly to the accreted mass due to the fact

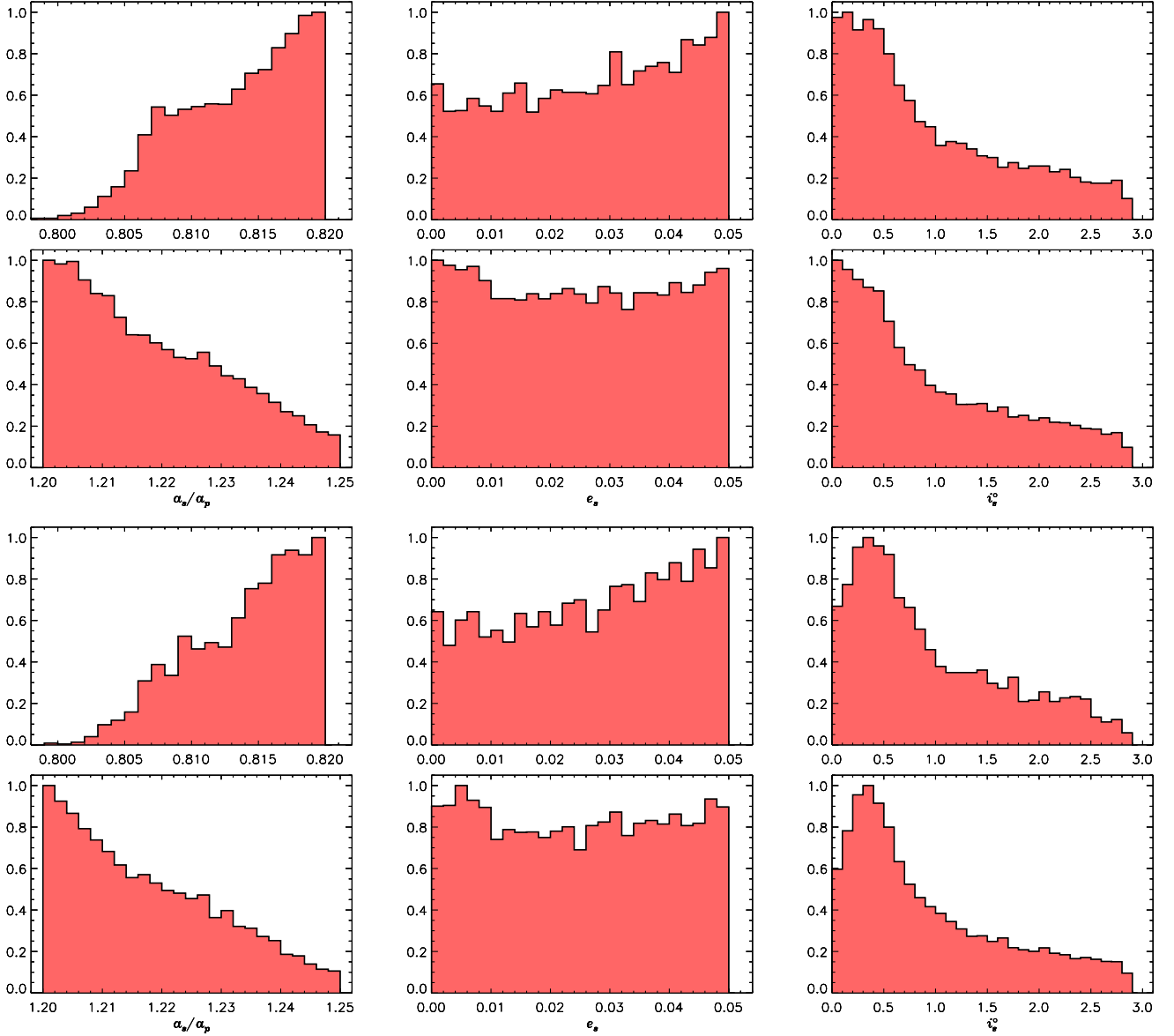


Figure 16. Initial distributions of semi-major axis (left), eccentricity (center), and inclination (right) of accreted planetesimals for $\rho_0 = 10^{-12}$ (upper pair of rows) and $10^{-11} \text{ g cm}^{-3}$ (lower pair of rows). The histograms refer to the initial distributions of both icy and mixed-composition bodies. Histograms are normalized so that the maximum is 1.

that most mass is delivered to the planet in the form of $R_s \sim 100 \text{ km}$ bodies, which rarely break up. But this effect depends on body size and gas density. As above, at $\rho_0 = 10^{-11} \text{ g cm}^{-3}$ (but not at the lower ρ_0), disruption of $1 \text{ km} \lesssim R_s \lesssim 10 \text{ km}$ planetesimals would significantly contribute to the accretion of solids, if fragments efficiently accreted on the planet.

8. DISCUSSION AND CONCLUSIONS

The results presented here show how planetesimals of various sizes, initially orbiting in three narrow radial regions ($\Delta r \approx 0.26\text{--}0.36 \text{ AU}$) around a star and in proximity of a Jupiter-mass planet, are scattered through the circumstellar disk and toward the planet. Scattering is dominated by three-body interactions (star-planet-planetesimal) while gas drag typically operates as a perturbing force. In some case, for $R_s \lesssim 0.1 \text{ km}$, gas drag

does determine planetesimal dynamics. As expected, the evolution of mixed-composition (ice/quartz with a 60% ice mass fraction) and icy planetesimals is similar in most thermodynamical aspects.

The surface temperature of planetesimals, T_s (defined in Section 3.2), evolves toward an equilibrium value ($dT_s/dt \approx 0$), which in absence of significant mass loss is such that (see Equation (15))

$$(T_s^{\text{eq}})^4 \approx T_g^4 + \frac{C_D}{32\sigma_{\text{SB}}} \frac{\rho_g}{\epsilon_s} |\mathbf{v}_g - \mathbf{v}_s|^3. \quad (38)$$

By using the approximation $|\mathbf{v}_s - \mathbf{v}_g| \approx \xi^2 a_s \Omega_K / 2$ with $\xi \approx H/r$ (which holds far from the planet's orbit, see Section 5 and Appendix B.1), the second term on the right-hand side of Equation (38) becomes $(\xi/2)^6 C_D / (4\sigma_{\text{SB}}) (\rho_g / \epsilon_s) (GM_*/a_s)^{3/2}$. In the calcula-

tions described here, this term is usually small compared to T_g^4 and thus $T_s^{\text{eq}} \approx T_g$. This conclusion is supported by the calculations. Vigorous mass loss tends to lower T_s relative to T_g (see Figure 13). The inverse of the timescale required to reach equilibrium, neglecting both frictional heating and cooling via latent heat release, is

$$\frac{1}{T_s} \left| \frac{dT_s}{dt} \right| \approx \frac{\epsilon_s}{\delta_s} \frac{\sigma_{\text{SB}} T_s^3}{\rho_s C_s} \left| 1 - \left(\frac{T_g}{T_s} \right)^4 \right|. \quad (39)$$

For a given deviation from equilibrium (T_g), this timescale is $\propto \delta_s/T_s^3 \propto \lambda_s/T_s^6$ (see Equation (14)) and increases with approaching equilibrium. Some numerical examples on the evolution of T_s toward equilibrium are shown in Appendix B.2. The situation is more complex for eccentric orbit bodies, as they experience a varying gas temperature along their orbit. Nonetheless, an equilibrium temperature can be reached if $|dT_s/dt|/T_s \ll \Omega_K$.

Results concerning the distributions of solids can be rescaled to an arbitrary surface density (in the radial regions of initial deployment), Σ_s , provided that collisions and encounters among bodies do not significantly alter their dynamics, i.e., that Σ_s remains relatively low, as it may be the case at the late epochs of giant planet formation (see Section 6.1). The ejection rate of mass out of the disk domain ($2 \text{ AU} \lesssim r \lesssim 20 \text{ AU}$) is $\sim 2 \times 10^{-5} (\Sigma_s/1 \text{ g cm}^{-2}) M_{\text{E}} \text{ yr}^{-1}$. In reality, most of these bodies are on orbits bound to the star when they cross the boundaries, and “ejection” generally classifies orbits whose perihelia (aphelia) are inside (outside) of r_{mn} (r_{mx}). Planetesimals are scattered from the interior to the exterior of the planet’s orbit at a rate of $\sim 5 \times 10^{-6} (\Sigma_s/1 \text{ g cm}^{-2}) M_{\text{E}} \text{ yr}^{-1}$, and in the opposite direction at a rate of $\sim 2 \times 10^{-5} (\Sigma_s/1 \text{ g cm}^{-2}) M_{\text{E}} \text{ yr}^{-1}$. These rates refer to scattered objects that have elliptical orbits about the star. Arguably, these scattering rates may only apply for a limited period of time, if solids are not replenished via collisions or some other mechanism (e.g., gravitational stirring or scattering by other planets). Therefore, the minimum masses that can be scattered out of boundaries, inside and outside the planet’s orbit are $\sim 0.25 (\Sigma_s/1 \text{ g cm}^{-2}) M_{\text{E}}$, $\sim 0.3 (\Sigma_s/1 \text{ g cm}^{-2}) M_{\text{E}}$, and $\sim 0.1 (\Sigma_s/1 \text{ g cm}^{-2}) M_{\text{E}}$, respectively (neglecting contributions from the mass in the corotation region).

For the disk temperatures applied here, both icy and mixed-composition bodies would be ablated inside $r \approx 2.8 \text{ AU}$ ($T_g = T_n \approx 220 \text{ K}$). However, disk models (e.g., D’Alessio et al. 2005) suggest lower temperatures after a few to several million years, hence ice-rich planetesimals may survive at radii $r \lesssim 2 \text{ AU}$. Regardless, scattering by a Jupiter-mass planet provides an important source of hydrated planetesimals to inner disk regions. A mass equal to the current mass of the main asteroid belt (Krasinsky et al. 2002) would be delivered in $\sim 50 (1 \text{ g cm}^{-2}/\Sigma_s) \text{ yr}$. These bodies would still orbit in a relatively dense gas, but the orbital decay time of $R_s \gtrsim 1 \text{ km}$ planetesimals around 2.5 AU would be $\gtrsim 5 \times 10^5$ local orbital periods for $\rho_0 \approx 10^{-11} \text{ g cm}^{-3}$. Orbital eccentricities and inclinations would be damped on timescales shorter by factors of ~ 200 .

The planetesimals orbiting in the corotation region $a_p \pm R_{\text{H}}$ are removed at an average rate of $\sim 6 \times$

$10^{-6} (\Sigma_s/1 \text{ g cm}^{-2}) M_{\text{E}} \text{ yr}^{-1}$. However, the tadpole orbits around the L_4 and L_5 points are very stable, due to low gas densities (see Figure 2), and number densities do not drop around these points. Since the rate of capture in the corotation region appears to be much smaller than the removal rate, the local density may bear information about dynamical and physical conditions at earlier times, before the giant planet acquires its massive envelope (see also Peale 1993).

The steep radial pressure gradient induced by the planet at the edges of the gap in the gas density profile (as function of r , see Figure 3) can partially prevent small planetesimals ($R_s \sim 0.1 \text{ km}$) from crossing the planet’s orbit, but this effect reduces as gas dissipates (see Figure 9). The size range most affected is determined by the strength of the drag acceleration (Equation (9)), and hence by $\partial P_g/\partial r$ at the gap’s outer edge. A condition for gap formation derived from the balance of viscous and tidal torques (D’Angelo & Marzari 2012, and references therein) is

$$\frac{1}{\sqrt{3\pi\alpha_g}} \left(\frac{M_p}{M_*} \right) \left(\frac{a_p}{H} \right) \left(\frac{a_p}{\tilde{\Delta}} \right)^{3/2} \gtrsim 1, \quad (40)$$

where $\tilde{\Delta} = \max(H, R_{\text{H}})$. The value of the left-hand side of this inequality is ≈ 5.6 for the parameters adopted here. A similar number is obtained for a Saturn-mass planet and somewhat smaller values for H/r and α_g , which suggests that a reduction in the inward flux of $R_s \sim 0.1 \text{ km}$ (and smaller) planetesimals may begin prior to reaching the current mass of Jupiter.

Experiments conducted on $1 \text{ cm} \leq R_s \leq 10 \text{ m}$ bodies, initially released exterior of the planet’s orbit ($1.2 < a_s/a_p < 1.25$), show that these particles remain segregated. After ~ 600 orbital periods of the planet, results indicate that the amount of solids delivered to the interior disk is negligible (for $\rho_0 = 10^{-12} \text{ g cm}^{-3}$) or virtually zero (for $\rho_0 = 10^{-11} \text{ g cm}^{-3}$). The radial position of the swarm’s inner edge is between $r \approx 1.27 a_p$ and $1.4 a_p$ for $1 \text{ cm} \lesssim R_s \lesssim 10 \text{ cm}$, and between $r \approx 1.36 a_p$ and $1.4 a_p$ for $1 \text{ m} \lesssim R_s \lesssim 10 \text{ m}$ (the position also depends on ρ_0). For $\rho_0 = 10^{-11} \text{ g cm}^{-3}$, particles of 1 cm in radius are halted at $r \approx 1.18 a_p$, close to the peak of super-Keplerian rotation in Figure 3. Segregation also leads to negligible fluxes of these bodies toward the circumplanetary disk. When $\rho_0 = 10^{-12} \text{ g cm}^{-3}$, we do find that 10 m -bodies can be scattered toward the planet and the inner disk when $a_s \approx 1.2 a_p$ and $e_s \approx i_s \approx 0$. However, this scattering event lasts only briefly at the beginning of the calculation, before the swarm recedes. Therefore, this is likely a transient effect induced by the choice of the initial distributions. Nonetheless, if $R_s \sim 10 \text{ m}$ bodies are produced via collisional comminution of planetesimals around $r = 1.2 a_p$, part of them may be scattered inward.

Planetesimals can be captured in the circumplanetary disk with a wide range of (planetocentric) orbits, including retrograde ones (see Figures 11 and 12) as also found by other recent studies (e.g., Fujita et al. 2013; Tanigawa et al. 2014). The ensemble of bodies with retrograde orbits comprises planetesimals with radii $0.1 \text{ km} \lesssim R_s \lesssim 100 \text{ km}$, although most of those coming from the exterior disk have $R_s \gtrsim 10 \text{ km}$. Capture of planetesimals provides

the circumplanetary disk with a time-averaged solids' reservoir of $\sim 10^{-3} (\Sigma_s/1 \text{ g cm}^{-2}) M_E$, which may be considered as a balance between the external supply and the loss due to ejection, ablation, break-up, and accretion on the planet. This amount of solids would account for a relatively low surface density (although planetesimals are continuously supplied), $\sim 0.3 \Sigma_s$, which may indicate relatively long times, $\sim 10^7 (1 \text{ g cm}^{-2}/\Sigma_s)$ local orbital periods about the planet, for the formation of $\sim 10^3$ km-radius satellites. Applied to the Galilean satellites, these formation times appear compatible with Callisto, which is partially undifferentiated (Stevenson et al. 1986), and may suggest post-formation differentiation of the inner three satellites (Schubert et al. 2004). Type I migration due to tidal interactions (e.g., Tanaka et al. 2002) with the thick circumplanetary disks considered here (see Figures 4 and 5) would lead to timescales for the orbital decay, at $\tilde{r} \sim 0.04 R_H$, of $\sim 10^9 (10^{-12} \text{ g cm}^{-3}/\rho_0)$ local orbital periods, longer than formation timescales.

Sustained ablation close to the planet ($\tilde{r} \lesssim 0.1 R_H$) releases heavy elements in the gas at a rate of $\sim 10^{-7} (\Sigma_s/1 \text{ g cm}^{-2}) M_E \text{ yr}^{-1}$, which is large enough to significantly alter the gas metallicity over relatively short timescales, possibly leading to a dust laden system. Disruption of planetesimals may also contribute to the solids' content of the circumplanetary disk.

Equation (37) approximates the accretion of solids on the planet supplied by a mono-size swarm of planetesimals, with radius in the range from ~ 1 km to ~ 100 km, where Σ_s is the solids' surface interior and exterior of the planet's orbit. Figure 16 indicates that the efficiency of accretion of planetesimals declines with increasing distance from the planet's orbit. If the edges of the gap in the solids' distribution are eroded, because of lack of supply or because they recede due to gas drag torques, the accretion rate is expected to decrease. Probably, late accretion of solids only represents a minor addition to the heavy element content of a giant planet (unless Σ_s is still quite large).

We estimate the mean accretion energy per unit mass, $\langle \Delta E_{\text{acc}}/\Delta M_s \rangle$, delivered to the planet by accreted planetesimals during the course of the calculations. The quantity ΔE_{acc} contains both kinetic and gravitational energy. We assume that all this energy is delivered close to the planet surface. The energy per unit time produced by accretion of solids is then

$$\langle \Delta E_{\text{acc}}/\Delta M_s \rangle \langle \dot{M}_p \rangle_s \sim 10^{-5} \left(\frac{\Sigma_s}{1 \text{ g cm}^{-2}} \right) L_\odot. \quad (41)$$

This accretion power can be compared to the planet's luminosity due to envelope contraction, between $\sim 10^{-6} L_\odot$ and $\sim 10^{-4} L_\odot$ (Lissauer et al. 2009). In reality, Equation (41) gives only a lower limit to the accretion power since additional energy is released as planetesimals sink into the planet. In fact, while ice dissolves at relatively shallow depths, where the temperature is $\lesssim T_{\text{cr}} \sim 650$ K, rock (which makes 40% of the mass of mixed-composition planetesimals) can sink to much deeper layers on account of the higher critical temperature ($T_{\text{cr}} = 4500$ K for quartz).

In some instances ($1 \text{ km} \lesssim R_s \lesssim 10 \text{ km}$ and $\rho_0 \sim 10^{-11} \text{ g cm}^{-3}$), planetesimal break-up in the circumplanetary disk produces significant amounts of solids that

may increase $\langle \dot{M}_p \rangle_s$ by factors of up to a few, if debris is accreted before being completely ablated (the dissolution timescale is $\propto R_s$, see Equation (33)). However, if break-up produces large (~ 0.1 km) fragments, ablation appears to dominate over accretion by a large margin: while $\sim 50\%$ of their mass is ablated, only $\sim 0.01\%$ is accreted. To examine more in detail the fate of smaller fragments, we present tests that use $1 \text{ cm} \leq R_s \leq 10 \text{ m}$ bodies as a proxy. These are released on circular orbits around the planet, between $\tilde{r} \approx 0.1 R_H$ and $\approx 0.6 R_H$, at the disk's equator. We find zero or negligible accretion. For radii $1 \text{ m} \lesssim R_s \lesssim 10 \text{ m}$, planetesimals migrate inward very quickly, but not enough to overcome ablation. Essentially, they are all ablated. At the reference density $\rho_0 \sim 10^{-12} \text{ g cm}^{-3}$, disruption of planetesimals releases less mass, but fragments can still be produced via collisional comminution. The same tests reveal similar conclusions. Bodies with radii $1 \text{ m} \lesssim R_s \lesssim 10 \text{ m}$ are almost entirely ablated without any significant amount being accreted. For comparison, $R_s \sim 0.1$ km planetesimals shed in the gas via ablation ≈ 30 times the mass they deliver to the planet via accretion.

Solids in the range $1 \text{ cm} \lesssim R_s \lesssim 10 \text{ cm}$, for both values of ρ_0 , are also much more prone to ablation than they are to accretion, if they move toward the planet. In the tests, none of these particles is accreted. In either case, the mass that is not ablated remains beyond $\tilde{r} \approx 0.1 R_H$ for the duration of the calculations, possibly because these small solids are more efficiently coupled to the gas than are larger particles and the gas radial velocity $\tilde{\mathbf{r}} \cdot \mathbf{v}_g/\tilde{r}$ (where \mathbf{v}_g is relative to the planet) is positive at the equator, i.e., directed away from the planet (see also Tanigawa et al. 2012). The conclusion is that small fragments resulting from disruption should not significantly contribute to accretion, but should rather contribute to the local reservoir of solids and to enriching the gas with heavy elements.

The main limitation of this study is the lack of planetesimal-planetesimal interactions, especially in the circumplanetary disk (see Section 6.1), which could affect the distribution of solids but which allows us to rescale the outcomes of the calculations to different values of the initial surface density of solids. The relatively short time span covered by the models is also a limiting factor. Another limitation is obviously the “discrete” approach, i.e., that of treating each particle as an individual body, which prevents from dealing with more realistic swarms of planetesimals, in terms of both number densities and size distributions. However, this approach allows us to model the evolution of the thermodynamical properties of single planetesimals at levels of detail not accessible to other, e.g., statistical or hybrid, approaches. Therefore, the method applied here can complement other techniques by providing detailed information on restricted populations of planetesimals at selected epochs of evolution.

We wish to express our gratitude to Jack Lissauer and Peter Bodenheimer for their valuable feedback. We thank an anonymous referee for prompt and constructive comments. G.D. acknowledges support from NASA Outer Planets Research Program grant 202844.02.02.01.75 and from NASA Origins of Solar Sys-

tems Program grants NNX11AD20G, NNX11AK54G, and NNX14AG92G. Resources supporting this work were provided by the NASA High-End Computing (HEC) Program through the NASA Advanced Supercomputing (NAS) Division at Ames Research Center.

APPENDIX

A. THE DRAG COEFFICIENT

Melosh & Goldin (2008) performed an extensive study of the literature on existing gas drag experiments (see, e.g., Walsh 1976, and references therein). They derived an expression for the drag coefficient C_D , in Equation (8) and (9), as a function of the Mach number \mathcal{M} (see Equation (10)), the Reynolds number \mathcal{R} (see Equation (11)), and their ratio $\mathcal{K} = \mathcal{M}/\mathcal{R}$. The function is continuous and extends over the entire (plausible) ranges of \mathcal{M} and \mathcal{R} .

Let us introduce the adiabatic gas sound speed

$$c_g = \sqrt{\gamma_g \frac{k_B T_g}{\mu_g m_H}}, \quad (\text{A1})$$

where γ_g is the adiabatic index of the gas (the isothermal sound speed is obtained for $\gamma_g = 1$) and the mean thermal velocity of the gas (e.g., Mihalas & Weibel Mihalas 1999)

$$\bar{v}_g = \sqrt{\frac{8}{\pi} \frac{k_B T_g}{\mu_g m_H}}, \quad (\text{A2})$$

which is the equivalent of Equation (18) for the gas constituents (atoms and/or molecules). Let us now define the magnitude of the relative velocity between the gas and a solid particle as $u = |\mathbf{v}_g - \mathbf{v}_s|$, then the (relative) Mach number can be written as

$$\mathcal{M} = \sqrt{\frac{8}{\pi \gamma_g}} \left(\frac{u}{\bar{v}_g} \right). \quad (\text{A3})$$

The definition of the relative Reynolds number in Equation (11) involves the dynamical molecular viscosity of the gas. If interactions among gas atoms/molecules can be described as collisions between two rigid elastic spheres, an approximation of the dynamical molecular viscosity is (Mihalas & Weibel Mihalas 1999)

$$\eta_g = \frac{5\sqrt{2}}{64} \left(\frac{m_H}{d_H} \right) \mu_g \bar{v}_g, \quad (\text{A4})$$

where m_H is the hydrogen mass and d_H is the typical diameter of the gas constituents. This length is $d_H = 2.71 \times 10^{-8}$ cm for hydrogen molecules and 2.15×10^{-8} cm for helium (Haynes 2011). Although the interaction model based on the rigid sphere representation of gas constituents, which interact only upon “contact”, is rather simple (see discussion in Mihalas & Weibel Mihalas 1999), Equation (A4) agrees within 25% with molecular hydrogen viscosity data (and 20% with helium) in the temperature range from 100 to 600 K (Haynes 2011).

By substituting Equations (A4) and (A3) into Equation (11), one finds that the (relative) Reynolds number can be cast into the following form

$$\mathcal{R} = \frac{32\sqrt{\pi}}{5} \left(\frac{d_H^2}{m_H} \right) \left(\frac{\sqrt{\gamma_g}}{\mu_g} \right) \rho_g R_s \mathcal{M}. \quad (\text{A5})$$

The ratio \mathcal{K} of the Mach number to the Reynolds number can also be written as

$$\mathcal{K} = \frac{5}{32\sqrt{\pi}} \left(\frac{m_H}{d_H^2} \right) \left(\frac{\mu_g}{\rho_g R_s \sqrt{\gamma_g}} \right). \quad (\text{A6})$$

It is important to note that \mathcal{K} is proportional to the Knudsen number, which is defined as the ratio between the mean-free path of a gas atom/molecule and the particle diameter. Therefore, \mathcal{K} may be regarded as a modified Knudsen number. The proportionality factor depends on the form adopted for the dynamical viscosity η_g (see PPR88). In our case, Equation (A4) yields a proportionality factor equal to $(16/5)\sqrt{\gamma_g/(2\pi)} \simeq 1.28\sqrt{\gamma_g}$.

In the derivation of Melosh & Goldin (2008), the drag coefficient is written as

$$C_D = 2 + (C_S - 2) e^{-p_1 \sqrt{\gamma_g} \mathcal{K} G(\mathcal{R})} + C_E e^{-1/(2\mathcal{K})}, \quad (\text{A7})$$

where

$$C_E = \frac{1}{\sqrt{\gamma_g} \mathcal{M}} \left(\frac{4.6}{1 + \mathcal{M}} + 1.7 \sqrt{\frac{T_s}{T_g}} \right), \quad (\text{A8})$$

and the auxiliary function $G(\mathcal{R})$ is such that

$$\log G = \frac{2.5 (\mathcal{R}/312)^{p_2}}{1 + (\mathcal{R}/312)^{p_2}}. \quad (\text{A9})$$

The constants p_1 in Equation (A7) and p_2 in Equation (A9) are $p_1 = 3.07$ and $p_2 = 0.6688$. The function $G(\mathcal{R})$ takes limiting values of 1, for $\mathcal{R} \rightarrow 0$, and of $10^{2.5} \approx 316.23$, for $\mathcal{R} \rightarrow \infty$.

For $\mathcal{K} \gg 1$, when the particle size is much smaller than the mean-free path of the gas constituents, a regime referred to as free-molecular flow, the drag coefficient takes the value

$$C_D \xrightarrow{\mathcal{K} \gg 1} C_E + 2, \quad (\text{A10})$$

which, for Mach numbers $\ll 1$, becomes $(4.6 + 1.7\sqrt{T_s/T_g})/(\sqrt{\gamma_g} \mathcal{M})$, as in the Epstein regime (e.g., Whipple 1973; Weidenschilling 1977). We stress here that Equation (A8) ought to be regarded as an extension of the Epstein drag coefficient (see Hood & Horanyi 1991 and discussion in Liffman & Toscano 2000). In fact, the form of Epstein coefficient typically adopted in the literature, $(8/3)\sqrt{8/(\pi\gamma_g)}/\mathcal{M}$ (e.g., Supulver & Lin 2000; Chiang & Youdin 2010, and references therein), only applies when there is specular reflection of the gas constituents impinging on the particle (see Epstein 1924, for details), which corresponds to assuming $T_s = 0$ in the limiting expression above. Epstein (1924, Part I, Section 7) also argued that, for $\mathcal{K} \gg 1$, particles should be considered as perfect thermal conductors, i.e., $T_s = T_g$, and the drag coefficient is then $(8/3 + \pi/3)\sqrt{8/(\pi\gamma_g)}/\mathcal{M}$, in agreement with the limiting expression above. At large Mach numbers, the right-hand side of Equation (A10) has asymptotic behavior $2 + (1.7/\mathcal{M})\sqrt{T_s/(\gamma_g T_g)}$ (e.g., Whipple 1950; Baker 1959).

For $\mathcal{K} \ll 1$, as happens in the continuum and incompressible ($\mathcal{M} \ll 1$) flow regimes, the first exponential in Equation (A7) tends to 1 while the second exponential tends to 0. Therefore, the drag coefficient takes the value

$$C_D \xrightarrow{\mathcal{K} \ll 1} C_S. \quad (\text{A11})$$

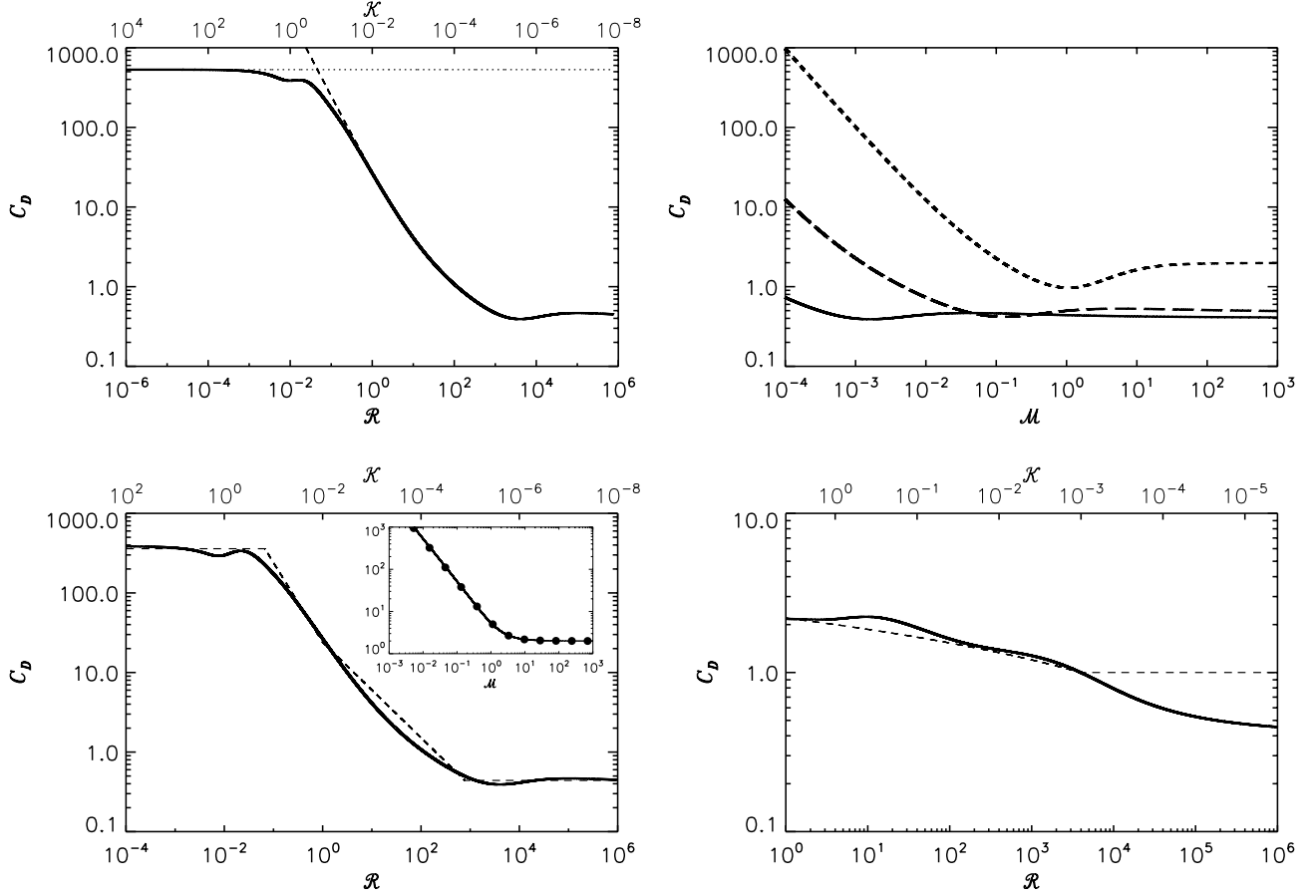


Figure 17. Top-left: the drag coefficient, C_D , given in Equation (A7), versus the Reynolds number, \mathcal{R} (bottom axis), and $\mathcal{K} = \mathcal{M}/\mathcal{R}$ (top axis), for $T_s = T_g$ and a Mach number $\mathcal{M} = 0.01$. The dotted line is the limit for $\mathcal{K} \gg 1$, given in Equation (A10). The dashed line is the limit for $\mathcal{K} \ll 1$, given in Equation (A12). Top-right: C_D as a function of the Mach number for particle of different radius: 10⁷ cm (solid line), 10⁵ cm (long-dashed line), and 10³ cm (short-dashed line). Bottom-left: The solid line is C_D from Equation (A7) while the dashed line is the drag coefficient used by Whipple (1973) and Weidenschilling (1977) (T_s is set to zero in Equation (A7), as discussed in the text). The inset shows a comparison with the drag coefficient used, among others, by Stalder & Zurick (1951); Probst (1968); Hood & Horanyi (1991); Tedeschi et al. (1999); Liffman & Toscano (2000) (solid circles), which applies for $\mathcal{K} \gg 1$. Bottom-right: as in the bottom-left panel, but the dashed line is the coefficient for $\mathcal{R} > 1$ and $\mathcal{M} > 1$ used by PPR88.

In this study, for C_S , we use a formula suggested by Brown & Lawler (2003)

$$C_S = \frac{24}{\mathcal{R}} (1 + 0.15\mathcal{R}^{p_3}) + \frac{0.407\mathcal{R}}{\mathcal{R} + 8710}, \quad (\text{A12})$$

in which the constant in the power of \mathcal{R} is $p_3 = 0.681$. For $\mathcal{R} \lesssim 1$, Equation (A12) becomes the classical Stokes drag law $C_S \approx 24/\mathcal{R}$ (e.g., Whipple 1973; Weidenschilling 1977; Brown & Lawler 2003), whereas, for $\mathcal{R} \gg 1$, we have that $C_S \approx 0.407$, sometimes referred to as the Newtonian drag coefficient (e.g., Whipple 1973). For non-spherical shapes, e.g., a cube or a short cylinder, this asymptotic value would be more than twice as large.

In the top panels of Figure 17, we plot the drag coefficient in Equation (A7) versus the Reynolds number (Equation (A5)) and the modified Knudsen number (Equation (A6)), and also display the two limiting cases in Equations (A10) and (A12). In the right panel, C_D is plotted for three different particle radii versus the Mach number. In the bottom panels, we make comparisons with drag coefficients used in previous studies (see figure caption for details), including the widely used coefficient

for free-molecular flows of Stalder & Zurick (1951, their Equations (A15) and (A17)).

B. TESTS ON SOLUTIONS OF THE PARTICLE EVOLUTION

In this Appendix, we present tests of the ordinary differential equation solver applied to the system of eight Equations (26), (4), (5), (6), (15), and (19) or (23). In order to make comparisons with compact analytic solutions, in the various tests we solve a reduced system and discuss separately dynamical problems (Equations (26) (4), (5), and (6)) in Appendix B.1 and thermodynamical problems (Equations (15) and (19) or (23)) in Appendix B.2.

B.1. Dynamics Tests

The solver is first tested against standard two-body problems, in which the particle orbits the star. Orbital energy and angular momentum are expected to be conserved in these problems and the extent to which this requirement is fulfilled provides an indication of accuracy.

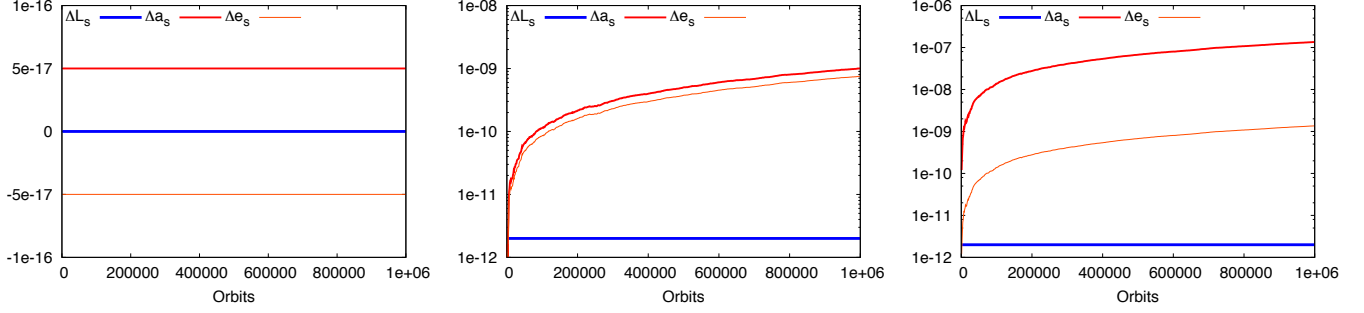


Figure 18. Variations of orbital angular momentum, semi-major axis and eccentricity in two-body problems with initial eccentricities 0 (left), 0.5 (center), and 0.99 (right). In the left panel, to separate the three curves, Δa_s and Δe_s are shifted by an amount equal to 5×10^{-17} . In the center and right panels, ΔL_s is zero within machine precision, hence it is shifted by 2×10^{-12} to appear in the plot.

Let us indicate with M_* the stellar mass, with M_s the particle mass, and with a_s and e_s the particle's semi-major axis and eccentricity. In a two-body problem, the orbital energy and angular momentum per unit mass are, respectively, $E_s = -G(M_* + M_s)/(2a_s)$ and

$$L_s = \sqrt{G(M_* + M_s)a_s(1 - e_s^2)}, \quad (\text{B1})$$

where G is the gravitational constant (here L_s should not be confused with the specific vaporization energy). Conservation of energy and angular momentum translates into constancy of a_s and e_s or of a_s and L_s . In fact, taking the differential of Equation (B1) and dividing by L_s^2 , we have

$$\frac{dL_s}{L_s} = \frac{1}{2} \frac{da_s}{a_s} - \left(\frac{e_s^2}{1 - e_s^2} \right) \frac{de_s}{e_s}, \quad (\text{B2})$$

which connects the relative variations of $\Delta L_s/L_s$, $\Delta a_s/a_s$, and $\Delta e_s/e_s$ (e.g., Beutler 2005).

Experiments indicate that an advantage of integrating the equation of motion in terms spherical polar coordinates and angular momenta, in place of the usual cartesian positions and velocities, is a substantial improvement in conservation of angular momenta and, typically, of energy. In the calculations reported in Figure 18, we consider orbits with eccentricities $e_s = 0$ (left), 0.5 (center), and 0.99 (right). In all cases L_s is conserved to machine precision, whereas the expected error in energy for the most eccentric orbit is one part in 10^4 over a period of 1 Gyr, as the asymptotic error is linear in time in that case (e.g., Calvo & Sanz-Serna 1993). If necessary, better conservation can be obtained by constraining the internal time step of the solver at the expense of an increased run time.

Another test we discuss is a circular restricted three-body problem, constituted by two massive bodies, whose masses are M_1 and M_2 , and a massless particle. All bodies orbit in the same plane and the radius of the massive bodies' orbit is a . The Jacobi's integral of motion for such system is (e.g., Murray & Dermott 2000)

$$C_J = \left[\frac{G(M_1 + M_2)}{a^3} \right] r^2 + 2 \left(\frac{GM_1}{r_1} + \frac{GM_2}{r_2} \right) - v^2, \quad (\text{B3})$$

where r and v are the distance and velocity of the particle relative to the center of mass of the massive bodies, and r_1 and r_2 are the distances relative to these bodies.

In Figure 19 (left), we set $M_1 + M_2 = 1$ and $M_2/M_1 =$

0.001. The Jacobi's integral is plotted as a function of the orbital period of M_2 around M_1 , for particles on tadpole (thicker curve), horseshoe, and circulating (thinner curve) orbits (see figure caption for details). While the error in the circulating orbit test displays a typical asymptotic linear behavior (usually due to truncation errors in the algorithm), no systematic errors appear in the solutions for the tadpole and horseshoe orbits.

In order to test the solver in the presence of drag, we follow the approach of Peale (1993). Consider a particle orbiting a star in gaseous disk. The rate of change of the particle's orbital energy is equal to the work done on it in the inertial frame, that is $M_s dE_s/dt = \mathbf{F}_D \cdot \mathbf{v}_s$, where \mathbf{F}_D is the drag force given by Equation (8). Differentiating the specific orbital energy E_s (see above), we have

$$\left[\frac{G(M_* + M_s)}{2a_s^2} \right] \left(\frac{da_s}{dt} \right) = \frac{3}{8} \frac{C_D}{R_s} \left(\frac{\rho_g}{\rho_s} \right) |\mathbf{v}_g - \mathbf{v}_s| \times (\mathbf{v}_g \cdot \mathbf{v}_s - |\mathbf{v}_s|^2). \quad (\text{B4})$$

For the sake of simplicity, the drag coefficient is taken to be constant, the disk's gas velocity is approximated as sub-Keplerian (due to support provided by the pressure gradient) with no radial component, and $|\mathbf{v}_s| \approx a_s \Omega_K$, where $\Omega_K^2 = G(M_* + M_s)/a_s^3$. Hence, we have that $|\mathbf{v}_s - \mathbf{v}_g| = a_s \Omega_K (1 - \sqrt{1 - \xi^2})$. The quantity ξ is connected to the gradients of temperature and surface density of the disk's gas, as well as to the disk's local thickness, H/r (see, e.g., Peale 1993; Takeuchi & Lin 2002; Tanaka et al. 2002), and is assumed to be constant. Under typical disk conditions, one finds that $\xi \sim H/r$ (see also Equation (27)). If we indicate with a_0 and Ω_0 the initial values of a_s and Ω_K , Equation (B4) can be written as

$$\frac{d}{dt} \left(\frac{a_s}{a_0} \right) = -\frac{1}{\tau} \left(1 - \sqrt{1 - \xi^2} \right)^2 \left(\frac{a_0}{a_s} \right)^b \sqrt{\frac{a_s}{a_0}}, \quad (\text{B5})$$

in which $1/\tau = (3/4)C_D(\rho_{g0}/\rho_s)(a_0/R_s)\Omega_0$ and $\rho_g = \rho_{g0}(a_0/a_s)^b$ with $b \geq 0$. The solution of Equation (B5) is

$$\frac{a_s}{a_0} = \left[1 - \left(\frac{1+2b}{2} \right) \left(1 - \sqrt{1 - \xi^2} \right)^2 \left(\frac{t}{\tau} \right) \right]^{2/(1+2b)}. \quad (\text{B6})$$

Our working assumptions imply that $|da_s/dt| \ll a_s \Omega_K (1 - \sqrt{1 - \xi^2})$ which, by using Equation (B5), be-

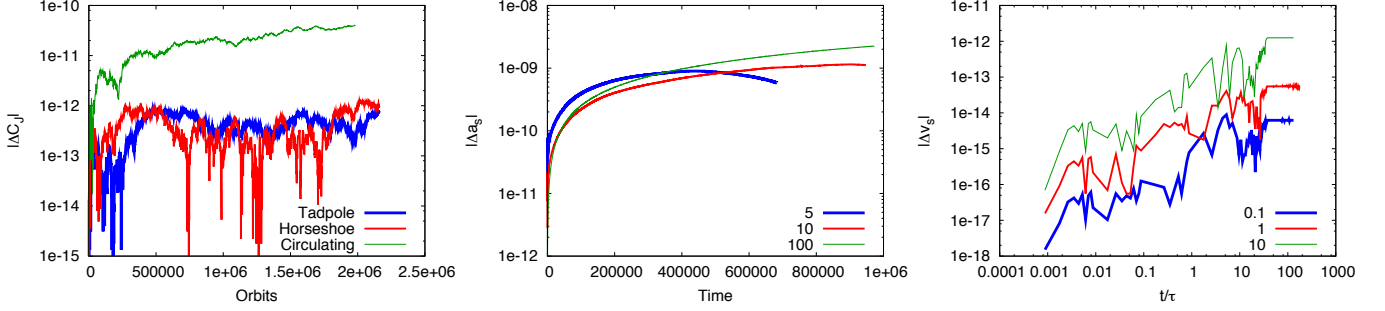


Figure 19. Left. Variation of the Jacobi's integral (Equation (B3)) versus the orbital period of the massive bodies. The three curves refer to particles on different types of orbits: tadpole (thicker line) horseshoe, and circulating (thinner line). Center. Difference $|\Delta a_s|$ between calculated and predicted positions of a particle subject to gas drag versus time in units of $2\pi/\Omega_0$. The predicted position is given by Equation (B6) with parameter $b = 0$. The three curves refer to different values of the constant $\Omega_0\tau$, as indicated in the legend (τ is defined after Equation (B5)). Right. Difference $|\Delta v_s|$ between calculated and predicted (Equation (B10)) velocities of a free-falling particle. The curves correspond to three values of the transient time τ (defined after Equation (B9)) in units of $1/\Omega_0$, as indicated in the legend.

comes $(a_0/\tau)(1 - \sqrt{1 - \xi^2})(a_0/a_s)^{b-1/2} \ll a_s\Omega_K$, or equivalently

$$\frac{3}{4}C_D \left(\frac{\rho_g}{\rho_s}\right) \left(\frac{a_0}{R_s}\right) \left(1 - \sqrt{1 - \xi^2}\right) \left(\frac{a_0}{a_s}\right)^{b-1} \ll 1. \quad (\text{B7})$$

If $\xi^2 \ll 1$ and $0 \leq b \lesssim 1$, the inequality (B7) becomes $(3/8)C_D(\rho_g/\rho_s)(a_0/R_s)\xi^2 \ll 1$.

In the center panel of Figure 19, we show results for the orbital evolution of a particle initially moving on a circular orbit and subject to gas drag. The difference Δa_s between the calculated position and that predicted by Equation (B6) is illustrated for three values of $\Omega_0\tau$, assuming a radially constant gas density ρ_g (i.e., $b = 0$).

We also present a test conducted on a classical free-fall problem. Consider a particle at some height above the equatorial plane of the disk and suppose that it is subject to a constant gravitational acceleration, g , directed toward the equatorial plane, and to gas drag (Equation (9)). Moreover, suppose that the particle's velocity, \mathbf{v}_s , is perpendicular to the disk's equatorial plane and that there is no vertical motion of the gas. The scalar acceleration of the particle is then

$$\frac{dv_s}{dt} = -g - \frac{3}{8} \left(\frac{C_D}{R_s} \frac{\rho_g}{\rho_s}\right) |v_s| v_s. \quad (\text{B8})$$

If $v_s > 0$, the acceleration is always negative, and eventually the velocity becomes first zero and then negative ($dv_s/dt < 0$ if $v_s = 0$). If $v_s \leq 0$, Equation (B8) can be written as

$$\frac{dv_s}{dt} = -g + \left(\frac{1}{4g\tau^2}\right) v_s^2, \quad (\text{B9})$$

where $1/(g\tau^2) = (3/2)(C_D/R_s)(\rho_g/\rho_s)$ and τ is a timescale. For $v_s < -2g\tau$, the acceleration is positive and negative otherwise. Thus, the particle will always approach the velocity $-2g\tau$, which is referred to as terminal or asymptotic velocity of the free-fall problem. The solution to Equation (B9) is

$$v_s = 2g\tau \left(\frac{1 \mp Be^{t/\tau}}{1 \pm Be^{t/\tau}}\right). \quad (\text{B10})$$

Quantity B is a *positive* integration constant determined through the initial condition. The top (bottom) signs in front of B apply if v_s^2 is smaller (larger) than $(2g\tau)^2$. In

the limit $t \rightarrow \infty$, either solution tends to the terminal velocity.

In the right panel of Figure 19, we plot the difference Δv_s between the calculated free-fall velocity of a particle (with zero initial velocity) and that predicted by Equation (B10) as a function of the normalized time t/τ . A velocity within 1% of the terminal velocity is attained for $t/\tau \gtrsim 5$.

B.2. Thermodynamics Tests

In this section, we test the numerical solution of reduced forms of Equation (12) against analytical solutions. We shall assume that heating and cooling processes affect the entire volume of the particle, which thus has a uniform temperature throughout. This assumption basically implies that the thermal conductivity of the body, λ_s , tends to infinity (see discussion in Section 3.2). We adopt this simplified approach here, instead of solving Equation (15), because it helps in searching for analytical solutions of the reduced equations.

Consider the situation in which the particle mass, M_s , is constant and the temperature of the gas, T_g , is always equal to T_s , the particle temperature. Hence, if the particle moves through gas around a star, it is constantly heated via friction so that its temperature changes in time according to

$$\frac{dT_s}{dt} = \frac{3}{32} \left(\frac{C_D\rho_g}{R_s\rho_s C_s}\right) |\mathbf{v}_g - \mathbf{v}_s|^3. \quad (\text{B11})$$

All quantities in parenthesis on the right-hand side are taken as constants. Following one of the problems in Section B.2, we assume that the gas is partially supported by pressure and has no radial velocity component, then $|\mathbf{v}_s - \mathbf{v}_g| = a_s\Omega_K(1 - \sqrt{1 - \xi^2})$, where the azimuthal velocity of the particle is equal to $a_s\Omega_K$. If the radial position of the particle is given by Equation (B6) with $b = 0$, Equation (B11) becomes

$$\frac{dT_s}{dt} = \frac{3}{32} \left(\frac{C_D\rho_g}{R_s\rho_s C_s}\right) \left(\frac{a_0\Omega_0\sqrt{c\tau}}{1 - ct/2}\right)^3 \quad (\text{B12})$$

where τ is defined beneath Equation (B5) and $c = (1 - \sqrt{1 - \xi^2})^2/\tau$. As above, a_0 and Ω_0 are the initial values of a_s and Ω_K . Note that condition (B7) applies since we are using Equation (B6). The solution of Equation (B12)

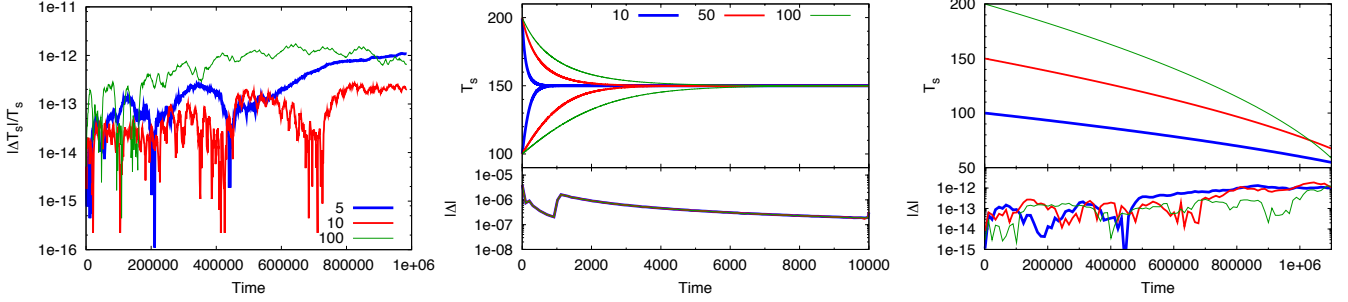


Figure 20. Left. Difference $|\Delta T_s|$ between calculated and predicted temperature of planetesimals, divided by the predicted temperature. Planetesimals are only heated via gas friction and cannot cool. The predicted temperature is given by Equation (B13). The curves refer to different values of the constant $\Omega_0\tau$, as indicated, and τ is defined after Equation (B5). See text for further details. Center. Temperature evolution of planetesimals heated by the gas radiation field and losing energy via radiative cooling. The gas temperature is fixed at $T_g = 150$ K. The initial temperature of the planetesimals is 100 K and 200 K and their radius in km is indicated in the legend. The lower panel shows the normalized difference between the numerical and the analytical solution (Equation (B15)). Right. Thermal evolution of planetesimals that lose energy due to ablation. The temperature is shown on the top while the normalized difference between numerical and analytical temperature (Equation (B19)) is shown on the bottom. In all panels, the time units are $2\pi/\Omega_0$.

is

$$T_s = T_s(0) + \frac{3}{32} \left(\frac{C_D \rho_g}{R_s \rho_s C_s} \right) (a_0 \Omega_0)^3 (c\tau)^{3/2} \times \left[\frac{1}{c(1 - ct/2)^2} - \frac{1}{c} \right]. \quad (\text{B13})$$

A Taylor expansion around $t = 0$ of the function in square brackets on the right-hand side gives t . The temperature diverges as $t \rightarrow 2/c$, i.e., as $a_s \rightarrow 0$, since the relative velocity $|\mathbf{v}_s - \mathbf{v}_g|$ diverges.

We solve Equation (B12) for different values of the constant $\Omega_0\tau$ and initial temperature of 100 K. In Figure 20 (left), we plot the difference $|\Delta T_s|$, between numerical and analytic solution (Equation (B13)), divided by the analytic solution. The rise in temperature is limited to a few degrees in case with longest τ and to over 50 K in the opposite case.

Consider another situation in which the particle has again a constant mass but its temperature differs from the gas temperature. Hence, the particle experiences heating by gas-emitted photons and cooling via back-body emission. Suppose also that the frictional heating is negligible or, otherwise stated, that the quantity in parenthesis on the right-hand side of Equation (B11) is vanishingly small. Thus, the temperature variation of the particle is governed by

$$\frac{dT_s}{dt} = 3 \left(\frac{\epsilon_s \sigma_{\text{SB}}}{R_s \rho_s C_s} \right) (T_g^4 - T_s^4). \quad (\text{B14})$$

Equation (B14) implies that the particle temperature evolves towards T_g , which is assumed to be constant. All quantities in first set of parenthesis on the right-hand side are also supposed to be constants. A solution to the equation is

$$\left(\frac{\epsilon_s \sigma_{\text{SB}}}{R_s \rho_s C_s} \right) t = I(T_s) - I(T_{s0}), \quad (\text{B15})$$

where T_{s0} is the initial particle temperature. For $T_s > T_g$, we have

$$I(T_s) = \frac{1}{4T_g^3} \left[\ln \left(\frac{T_s + T_g}{T_s - T_g} \right) + 2 \arctan \left(\frac{T_s}{T_g} \right) \right] \quad (\text{B16})$$

whereas for $T_s < T_g$, the function is

$$I(T_s) = \frac{1}{4T_g^3} \left[\ln \left(\frac{T_g + T_s}{T_g - T_s} \right) + 2 \arctan \left(\frac{T_s}{T_g} \right) \right]. \quad (\text{B17})$$

Equation (B15) defines implicitly T_s as a function of time.

Equation (B14) is solved numerically for three different radii (see figure caption) of planetesimals, orbiting a star with a period $2\pi/\Omega_0$. Two values of the initial planetesimal temperatures are applied: 100 K and 200 K, so that the bodies will either heat up or cool down toward the gas temperature of 150 K. The results are shown in the center panel of Figure 20, which illustrates T_s (top) and the normalized difference between numerical and analytical solutions (bottom) versus time.

Finally, we discuss a test in which a particle is neither subject to frictional heating (as in the first test of this section) nor to radiative heating and cooling (as in the second test). We assume that a particle loses mass, due to ablation, releasing vaporization energy in the process. For simplicity, the variation of the particle mass is such that dR_s/dt is constant, so that $dM_s/dt \propto R_s^2$. Thus, the energy budget reduces to

$$C_s(T_s) \frac{dT_s}{dt} = \left(\frac{L_s}{M_s} \right) \frac{dM_s}{dt}, \quad (\text{B18})$$

where, L_s , the specific energy of vaporization, is constant (see PPR88). The specific heat has the form $C_s = cT^b$ ($b \approx 1$), which is an approximation to the specific heat of ice between 30 K and 273 K (Haynes 2011). The solution to Equation (B18) is

$$T_s = \left[T_{s0}^{b+1} + 3 \left(\frac{b+1}{c} \right) L_s \ln \left(\frac{R_s}{R_{s0}} \right) \right]^{1/(b+1)}, \quad (\text{B19})$$

where T_{s0} and R_{s0} are the initial temperature and radius of the particle.

The right panel of Figure 20 shows the thermal evolution of particles that ablate and lose energy. Again, it is assumed that the particle orbits the star with a period $2\pi/\Omega_0$. Tests are performed for various values T_{s0} and R_{s0} . The temperature is illustrated on top while the normalized difference between the computed and the an-

alytical temperature in Equation (B19) is shown on the bottom of the figure.

REFERENCES

- Adachi, I., Hayashi, C., & Nakazawa, K. 1976, *Progress of Theoretical Physics*, 56, 1756 [13](#)
- Alibert, Y., Mousis, O., Mordasini, C., & Benz, W. 2005, *ApJ*, 626, L57 [8](#)
- Ayliffe, B. A., & Bate, M. R. 2009, *MNRAS*, 397, 657 [10](#)
- . 2012, *MNRAS*, 427, 2597 [8](#)
- Ayliffe, B. A., Laibe, G., Price, D. J., & Bate, M. R. 2012, *MNRAS*, 423, 1450 [15](#)
- Baker, Jr., R. M. L. 1959, *ApJ*, 129, 826 [24](#)
- Baldwin, B., & Sheaffer, Y. 1971, *J. Geophys. Res.*, 76, 4653 [6](#)
- Bate, M. R., Lubow, S. H., Ogilvie, G. I., & Miller, K. A. 2003, *MNRAS*, 341, 213 [8](#)
- Bell, C. P. M., Naylor, T., Mayne, N. J., Jeffries, R. D., & Littlefair, S. P. 2013, *MNRAS*, 434, 806 [8](#)
- Benz, W., & Asphaug, E. 1999, *Icarus*, 142, 5 [6](#)
- Beutler, G. 2005, *Methods of Celestial Mechanics. Vol. I: Physical, Mathematical, and Numerical Principles* (Berlin: Springer) [26](#)
- Biele, J., Ulamec, S., Richter, L., Kührt, E., Knollenberg, J., Möhlmann, D., & Philae Team. 2009, in *Deep Impact as a World Observatory Event: Synergies in Space, Time, and Wavelength*, ed. H. U. Käufl & C. Sterken (Berlin: Springer), 285 [6](#)
- Blottner, F. G. 1971, *NASA Special Publication* 252, 219 [5](#)
- Bodenheimer, P., Laughlin, G., Rózycka, M., & Yorke, H. 2006, *Numerical Methods in Astrophysics: An Introduction* (Boca Raton, FL: CRC Press, Taylor & Francis Group) [8](#)
- Bodenheimer, P., & Pollack, J. B. 1986, *Icarus*, 67, 391 [8](#)
- Boss, A. P., & Myhill, E. A. 1992, *ApJS*, 83, 311 [7](#)
- Brent, R. P. 1973, *Algorithms for Minimization Without Derivatives* (Englewood Cliffs, NJ: Prentice-Hall, Inc.) [11](#)
- Bromley, B. C., & Kenyon, S. J. 2011, *ApJ*, 731, 101 [1](#)
- Brown, P., & Lawler, D. 2003, *Journal of Environmental Engineering*, 129, 222 [3, 25](#)
- Calvo, M., & Sanz-Serna, J. 1993, *SIAM Journal on Scientific Computing*, 14, 936 [26](#)
- Campbell-Brown, M. D., & Koschny, D. 2004, *A&A*, 418, 751 [5](#)
- Canup, R. M., & Ward, W. R. 2002, *AJ*, 124, 3404 [11](#)
- . 2009, in *Europa*, ed. R. T. Pappalardo, W. B. McKinnon, & K. K. Khurana (Tucson, AZ: University Arizona Press), 59 [1](#)
- Cepilecha, Z. 1993, *LPI Contributions*, 810, 56 [6](#)
- Chase, M. W. 1998, *Journal of Physical and Chemical Reference Data*, 9, 1 [5](#)
- Chiang, E., & Youdin, A. N. 2010, *Annual Review of Earth and Planetary Sciences*, 38, 493 [24](#)
- Cox, G. F. N., & Richter-Menge, J. A. 1985, in *Proc. 4th Int'l Symposium on Offshore Mechanics and Arctic Engineering* (Dallas, TX), 1 [6](#)
- D'Alessio, P., Calvet, N., & Hartmann, L. 2001, *ApJ*, 553, 321 [11](#)
- D'Alessio, P., Merín, B., Calvet, N., Hartmann, L., & Montesinos, B. 2005, *Rev. Mexicana Astron. Astrofis.*, 41, 61 [16, 22](#)
- D'Angelo, G., Bate, M. R., & Lubow, S. H. 2005, *MNRAS*, 358, 316 [7](#)
- D'Angelo, G., Henning, T., & Kley, W. 2002, *A&A*, 385, 647 [7](#)
- . 2003a, *ApJ*, 599, 548 [7, 10](#)
- D'Angelo, G., Kley, W., & Henning, T. 2003b, *ApJ*, 586, 540 [8](#)
- D'Angelo, G., & Lubow, S. H. 2008, *ApJ*, 685, 560 [3, 8](#)
- D'Angelo, G., & Marzari, F. 2012, *ApJ*, 757, 50 [8, 16, 22](#)
- D'Angelo, G., Weidenschilling, S. J., Lissauer, J. J., & Bodenheimer, P. 2014, *Icarus*, 241, 298 [1](#)
- de Val-Borro, M., Artymowicz, P., D'Angelo, G., & Peplinski, A. 2007, *A&A*, 471, 1043 [7](#)
- de Val-Borro, M., Edgar, R. G., Artymowicz, P., Cieliegl, P., Cresswell, P., D'Angelo, G., Delgado-Donate, E. J., Dirksen, G., Fromang, S., Gawryszczak, A., Klahr, H., Kley, W., Lyra, W., Masset, F., Mellema, G., Nelson, R. P., Paardekoooper, S., Peplinski, A., Pierens, A., Plewa, T., Rice, K., Schäfer, C., & Speith, R. 2006, *MNRAS*, 370, 529 [7](#)
- Eggleton, P. P. 1983, *ApJ*, 268, 368 [3](#)
- Epstein, P. S. 1924, *Physical Review*, 23, 710 [24](#)
- Estrada, P. R., Mosqueira, I., Lissauer, J. J., D'Angelo, G., & Cruikshank, D. P. 2009, in *Europa*, ed. R. T. Pappalardo, W. B. McKinnon, & K. K. Khurana (Tucson, AZ: University Arizona Press), 27 [1](#)
- Fujita, T., Ohtsuki, K., Tanigawa, T., & Suetsugu, R. 2013, *AJ*, 146, 140 [22](#)
- Goldreich, P., & Tremaine, S. 1980, *ApJ*, 241, 425 [8](#)
- Greenzweig, Y., & Lissauer, J. J. 1990, *Icarus*, 87, 40 [12](#)
- Gressel, O., Nelson, R. P., Turner, N. J., & Ziegler, U. 2013, *ApJ*, 779, 59 [8](#)
- Hairer, E., Nørsett, S. P., & Wanner, G. 1993, *Solving Ordinary Differential Equations I: Nonstiff Problems* (Berlin: Springer) [7](#)
- Haisch, K. E., Lada, E. A., & Lada, C. J. 2001, *ApJ*, 553, L153 [8](#)
- Haynes, W. M., ed. 2011, *CRC Handbook of Chemistry and Physics*, 92nd edn. (Boca Raton, FL: CRC Press) [5, 24, 28](#)
- Holsapple, K. A. 2009, *Planet. Space Sci.*, 57, 127 [6](#)
- Hood, L. L., & Horanyi, M. 1991, *Icarus*, 93, 259 [6, 24, 25](#)
- Housen, K. R., & Holsapple, K. A. 1999, *Icarus*, 142, 21 [6](#)
- Hubickyj, O., Bodenheimer, P., & Lissauer, J. J. 2005, *Icarus*, 179, 415 [1, 8](#)
- Iaroslavitz, E., & Podolak, M. 2007, *Icarus*, 187, 600 [1](#)
- Inaba, S., Wetherill, G. W., & Ikoma, M. 2003, *Icarus*, 166, 46 [1](#)
- Jensen, J., Tuttle, W., Stewart, R., Brechna, H., & Prodell, A. 1980, *Selected Cryogenic Data Notebook* (Upton, NY: Brookhaven National Laboratory) [5](#)
- Jewitt, D., & Haghighipour, N. 2007, *ARA&A*, 45, 261 [10](#)
- Jewitt, D. C., Sheppard, S., & Porco, C. 2004, in *Jupiter. The Planet, Satellites and Magnetosphere*, ed. F. Bagenal, T. E. Dowling, & W. B. McKinnon (Cambridge, UK: Cambridge University Press), 263 [10](#)
- Kobayashi, H., Tanaka, H., Krivov, A. V., & Inaba, S. 2010, *Icarus*, 209, 836 [1](#)
- Kopal, Z. 1959, *Close Binary Systems* (London: Chapman & Hall) [3](#)
- Kopal, Z., ed. 1978, *Dynamics of Close Binary Systems* (Dordrecht: Reidel) [2, 3, 6](#)
- Krasinsky, G. A., Pitjeva, E. V., Vasilyev, M. V., & Yagudina, E. I. 2002, *Icarus*, 158, 98 [22](#)
- Lange, M. A., & Ahrens, T. J. 1983, *J. Geophys. Res.*, 88, 1197 [6](#)
- Lienhard, J. H., & Lienhard, J. H. 2008, *A Heat Transfer Textbook* (Cambridge, MA: Phlogiston Press) [4](#)
- Liffman, K., & Toscano, M. 2000, *Icarus*, 143, 106 [24, 25](#)
- Lin, D. N. C., & Papaloizou, J. 1986, *ApJ*, 307, 395 [8](#)
- Lissauer, J. J., Hubickyj, O., D'Angelo, G., & Bodenheimer, P. 2009, *Icarus*, 199, 338 [1, 7, 8, 10, 23](#)
- Lissauer, J. J., & Stewart, G. R. 1993, in *Protostars and Planets III*, ed. E. H. Levy & J. I. Lunine (Tucson, AZ: University Arizona Press), 1061 [12](#)
- Love, S. G., & Brownlee, D. E. 1991, *Icarus*, 89, 26 [4](#)
- Lubow, S. H., & D'Angelo, G. 2006, *ApJ*, 641, 526 [7](#)
- Lunine, J. I., & Stevenson, D. J. 1982, *Icarus*, 52, 14 [10](#)
- Machida, M. N., Kokubo, E., Inutsuka, S.-i., & Matsumoto, T. 2008, *ApJ*, 685, 1220 [10](#)
- Marley, M. S., Fortney, J. J., Hubickyj, O., Bodenheimer, P., & Lissauer, J. J. 2007, *ApJ*, 655, 541 [10](#)
- Martin, R. G., & Lubow, S. H. 2011, *MNRAS*, 413, 1447 [10](#)
- Masset, F. S., D'Angelo, G., & Kley, W. 2006, *ApJ*, 652, 730 [7](#)
- McAuliffe, J. P., & Christou, A. A. 2006, *Icarus*, 180, 8 [4](#)
- Melosh, H. J., & Goldin, T. J. 2008, *LPI Contributions*, 1391, 2457 [3, 24](#)
- Mihalas, D., & Weibel Mihalas, B. 1999, *Foundations of Radiation Hydrodynamics* (New York: Dover) [5, 7, 24](#)
- Mordasini, C., Alibert, Y., Klahr, H., & Benz, W. 2011, in *Detection and Dynamics of Transiting Exoplanets*, ed. F. Bouchy, R. Díaz & C. Moutou (EPJ Web of Conferences), 11, 4001 [8](#)
- Mosqueira, I., Estrada, P. R., & Charnoz, S. 2010, *Icarus*, 207, 448 [5](#)
- Mousis, O., Choukroun, M., Lunine, J. I., & Sotin, C. 2014, *Icarus*, 239, 39 [1](#)
- Movshovitz, N., Bodenheimer, P., Podolak, M., & Lissauer, J. J. 2010, *Icarus*, 209, 616 [1, 8](#)
- Movshovitz, N., & Podolak, M. 2008, *Icarus*, 194, 368 [1](#)
- Murray, C. D., & Dermott, S. F. 2000, *Solar System Dynamics* (Cambridge, UK: Cambridge University Press) [2, 14, 26](#)
- Ogihara, M., & Ida, S. 2009, *ApJ*, 699, 824 [13](#)
- Paczynski, B. 1971, *ARA&A*, 9, 183 [3](#)
- Pascucci, I., Gorti, U., Hollenbach, D., Najita, J., Meyer, M. R., Carpenter, J. M., Hillenbrand, L. A., Herczeg, G. J., Padgett, D. L., Mamajek, E. E., Silverstone, M. D., Schlingman, W. M., Kim, J. S., Stobie, E. B., Bouwman, J., Wolf, S., Rodmann, J., Hines, D. C., Lunine, J., & Malhotra, R. 2006, *ApJ*, 651, 1177 [8](#)
- Peale, S. J. 1993, *Icarus*, 106, 308 [14, 22, 26](#)
- Petrovic, J. J. 2001, *Journal of Materials Science*, 36, 1579 [6](#)
- . 2003, *Journal of Materials Science*, 38, 1 [6](#)
- Podolak, M., Pollack, J. B., & Reynolds, R. T. 1988, *Icarus*, 73, 163 (PPR88) [4, 5, 6, 24, 25, 28, 29](#)
- Pollack, J. B., Burns, J. A., & Tauber, M. E. 1979, *Icarus*, 37, 587 [6](#)
- Pollack, J. B., Hollenbach, D., Beckwith, S., Simonelli, D. P., Roush, T., & Fong, W. 1994, *ApJ*, 421, 615 [11](#)
- Pollack, J. B., Hubickyj, O., Bodenheimer, P., Lissauer, J. J., Podolak, M., & Greenzweig, Y. 1996, *Icarus*, 124, 62 [1](#)
- Pollack, J. B., Podolak, M., Bodenheimer, P., & Christofferson, B. 1986, *Icarus*, 67, 409 [6](#)

- Popova, O., Borovička, J., Hartmann, W. K., Spurný, P., Gnoss, E., Nemtchinov, I., & Trigo-Rodríguez, J. M. 2011, *Meteoritics and Planetary Science*, 46, 1525 [6](#)
- Powell, R. W., Ho, C. Y., & Liley, P. E. 1966, *Thermal Conductivity of Selected Materials*, 8th edn. (Washington, D.C.: U.S. Dept. of Commerce, National Bureau of Standards), 175 [5](#)
- Prialnik, D., Benkhoff, J., & Podolak, M. 2004, in *Comets II*, ed. M. C. Festou, H. U. Keller, & H. A. Weaver (Tucson, AZ: University of Arizona Press), 359 [5](#)
- Pringle, J. E. 1981, *ARA&A*, 19, 137 [10](#)
- Probstein, R. F. 1968, in *Problems of Hydrodynamics and Continuum Mechanics*, ed. M. A. Lavret'ev et al. (Philadelphia, PA: SIAM), 568 [25](#)
- Roberge, A., & Kamp, I. 2011, in *Exoplanets*, ed. S. Seager (Tucson, AZ: University of Arizona Press), 269 [8](#)
- Schubert, G., Anderson, J. D., Spohn, T., & McKinnon, W. B. 2004, in *Jupiter. The Planet, Satellites and Magnetosphere*, ed. F. Bagenal, T. E. Dowling, & W. B. McKinnon (Cambridge, UK: Cambridge University Press), 281 [23](#)
- Shakura, N. I., & Syunyaev, R. A. 1973, *A&A*, 24, 337 [2](#)
- Stalder, J. R., & Zurick, V. J. 1951, *Theoretical Aerodynamic Characteristics of Bodies in a Free-Molecule-Flow Field* (Moffett Field, CA: NACA Ames Aeronautical Laboratory) [25](#)
- Stevenson, D. J., Harris, A. W., & Lunine, J. I. 1986, in *Satellites*, ed. J. A. Burns & M. S. Matthews (Tucson, AZ: University Arizona Press), 39 [23](#)
- Stewart, G. R., & Kaula, W. M. 1980, *Icarus*, 44, 154 [16](#)
- Stone, J. M., & Norman, M. L. 1992, *ApJS*, 80, 753 [7](#)
- Supulver, K. D., & Lin, D. N. C. 2000, *Icarus*, 146, 525 [24](#)
- Szulágyi, J., Morbidelli, A., Crida, A., & Masset, F. 2014, *ApJ*, 782, 65 [8](#)
- Takeuchi, T., & Lin, D. N. C. 2002, *ApJ*, 581, 1344 [26](#)
- Tanaka, H., Takeuchi, T., & Ward, W. R. 2002, *ApJ*, 565, 1257 [9](#), [23](#), [26](#)
- Tanigawa, T., Maruta, A., & Machida, M. N. 2014, *ApJ*, 784, 109 [22](#)
- Tanigawa, T., Ohtsuki, K., & Machida, M. N. 2012, *ApJ*, 747, 16 [8](#), [10](#), [23](#)
- Tedeschi, G., Gouin, H., & Elena, M. 1999, *Experiments in Fluids*, 26, 288 [25](#)
- Toth, I., & Lisse, C. M. 2006, *Icarus*, 181, 162 [6](#)
- van Leer, B. 1977, *Journal of Computational Physics*, 23, 276 [7](#)
- Wagner, W., & Pruß, A. 2002, *Journal of Physical and Chemical Reference Data*, 31, 387 [5](#)
- Walsh, M. 1976, *Influence of Particle Drag Coefficient on Particle Motion in High-Speed Flow With Typical Laser Velocimeter Applications* (Hampton, VA: NASA Langley Research Center) [24](#)
- Washburn, E. W. 1924, *Monthly Weather Review*, 52, 488 [5](#)
- Weidenschilling, S. J. 1977, *MNRAS*, 180, 57 [24](#), [25](#)
- Whipple, F. L. 1950, *Proceedings of the National Academy of Science*, 36, 687 [4](#), [24](#)
- . 1973, *NASA Special Publication*, 319, 355 [24](#), [25](#)
- Williams, J. P., & Cieza, L. A. 2011, *ARA&A*, 49, 67 [8](#)